



Rheologic and structural controls on the deformation of Okmok volcano, Alaska: FEMs, InSAR, and ambient noise tomography

Timothy Masterlark,¹ Matthew Haney,^{2,3} Haylee Dickinson,¹ Tom Fournier,^{4,5} and Cheryl Searcy²

Received 23 January 2009; revised 5 August 2009; accepted 13 October 2009; published 27 February 2010.

[1] Interferometric synthetic aperture radar (InSAR) data indicate that the caldera of Okmok volcano, Alaska, subsided more than a meter during its eruption in 1997. The large deformation suggests a relatively shallow magma reservoir beneath Okmok. Seismic tomography using ambient ocean noise reveals two low-velocity zones (LVZs). The shallow LVZ corresponds to a region of weak, fluid-saturated materials within the caldera and extends from the caldera surface to a depth of 2 km. The deep LVZ clearly indicates the presence of the magma reservoir beneath Okmok that is significantly deeper (>4 km depth) compared to previous geodetic-based estimates (3 km depth). The deep LVZ associated with the magma reservoir suggests magma remains in a molten state between eruptions. We construct finite element models (FEMs) to simulate deformation caused by mass extraction from a magma reservoir that is surrounded by a viscoelastic rind of country rock embedded in an elastic domain that is partitioned to account for the weak caldera materials observed with tomography. This configuration allows us to reduce the estimated magma reservoir depressurization to within lithostatic constraints, while simultaneously maintaining the magnitude of deformation required to predict the InSAR data. More precisely, the InSAR data are best predicted by an FEM simulating a rind viscosity of 7.5×10^{16} Pa s and a mass flux of -4.2×10^9 kg/d from the magma reservoir. The shallow weak layer within the caldera provides a coeruption stress regime and neutral buoyancy horizon that support lateral magma propagation from the central magma reservoir to extrusion near the rim of the caldera.

Citation: Masterlark, T., M. Haney, H. Dickinson, T. Fournier, and C. Searcy (2010), Rheologic and structural controls on the deformation of Okmok volcano, Alaska: FEMs, InSAR, and ambient noise tomography, *J. Geophys. Res.*, *115*, B02409, doi:10.1029/2009JB006324.

1. Introduction

[2] The internal rheologic structure, loading processes, and effective boundary conditions of a volcano control the physical fields, e.g., deformation, that we observe at the Earth's surface. Forward models of these internal structures and processes allow us to predict the surface fields. In practice, we are faced with the inverse situation of using surface observations to characterize the inaccessible internal structures and processes. Distortions of these characteristics are tied to our ability to (1) identify and resolve the internal rheologic structure, (2) simulate the internal processes

over a problem domain having this internal structure, and (3) calibrate these internal processes to the observed fields at the Earth's surface. For example, the net behavior of a deformation system driven by magmatic intrusion (or extrusion) is a synthesis of both static and transient processes that depend on the coupling of the internal loading and the rheologic structure. Conceptually, a pulse of strain gradually propagates away from a relatively instantaneous magma intrusion event and creates stress and strain fields that are functions of space, time, and the magnitude and geometry of the perturbation. By measuring and modeling these perturbations, we can iteratively test hypotheses of coeruption and posteruption behavior.

[3] The magnitude and scale of the observed deformation for the 1997 eruption of Okmok volcano, Alaska (Figure 1), provides an opportunity to conduct an in situ rheological experiment. The coeruption extraction of magma from a shallow reservoir is the impulse, and the subsequent deformation is the response. By simulating the impulse, measuring the response, and interpreting the constitutive relations that link the two, we can constrain in situ rheology. We present an analysis of observed deformation for the 1997 eruption of Okmok volcano using numerical models that simulate the

¹Department of Geological Sciences, University of Alabama, Tuscaloosa, Alabama, USA.

²Alaska Volcano Observatory, U.S. Geological Survey, Anchorage, Alaska, USA.

³Now at Geosciences Department, Boise State University, Boise, Idaho, USA.

⁴Geophysical Institute, University of Alaska Fairbanks, Fairbanks, Alaska, USA.

⁵Now at Department of Earth and Atmospheric Sciences, Cornell University, Ithaca, New York, USA.

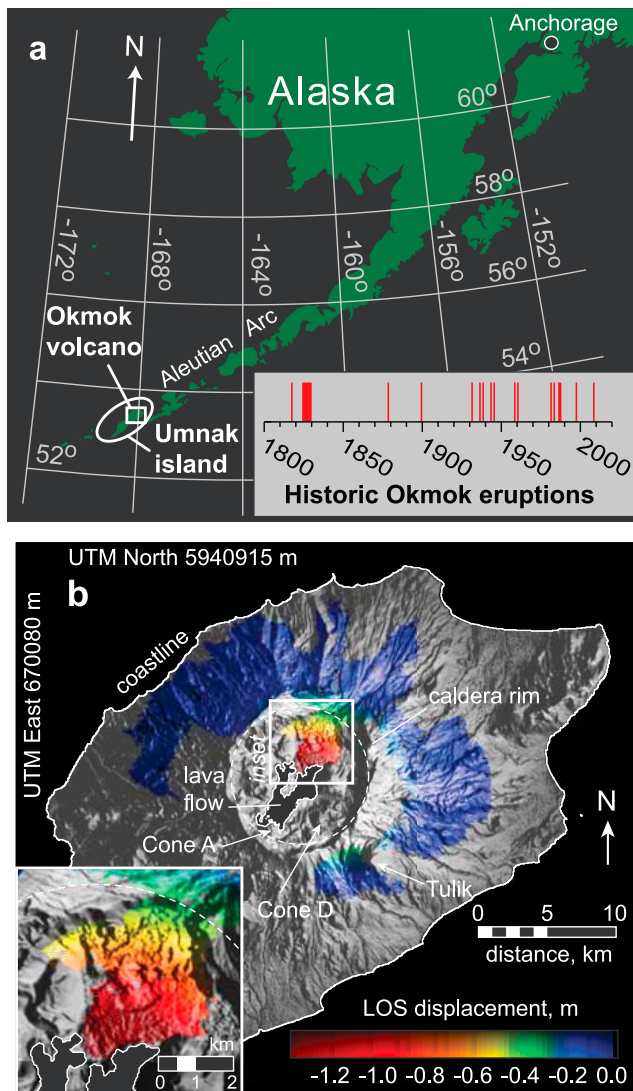


Figure 1. Okmok volcano, Alaska. (a) Location and eruption history. Okmok volcano occupies the northeast lobe of Umnak Island, Alaska. The eruption history is shown on the lower right. Each red bar represents a recorded eruption [Miller *et al.*, 1998]. Thick bars represent eruptions that span multiple years. (b) The 10 km diameter caldera dominates the shaded relief image of a digital elevation model. The lava flow from the 1997 eruption originated from Cone A. The recent 2008 eruption emanated from craters near Cone D. Unwrapped InSAR data reveal subsidence associated with the 1997 eruption of Okmok volcano. Positive LOS displacement of the land surface is toward the satellite. The pattern of negative displacement is indicative of volcano-wide deflation. Note the symmetry of the deformation pattern about the center of the caldera, for which the maximum LOS displacement is about -1.4 m. The inset reveals details of the caldera deformation.

transient response of a volcano deformation system due to magmatic flux from a shallow reservoir. The deformation models are designed to honor the available geologic and geophysical data in an effort to minimize the distortions attributed to somewhat overly simplified conventional half-

space models [e.g., Mogi, 1958] for Okmok and provide an innovative view of the internal processes of an active volcano.

[4] The Aleutian volcanic arc of the north Pacific hosts more than 40 active volcanoes [Begét *et al.*, 2005]. This 3000 km long volcanic arc extends westward from mainland Alaska to Kamchatka and formed as a result of subduction of the Pacific plate beneath the overriding North American plate [Finney *et al.*, 2008]. The convergence is orthogonal near the eastern end of the volcanic arc and transitions to almost pure strike-slip along the western end of the arc [Cross and Freymueller, 2008; Lallement and Oldow, 2000]. Rock compositions along the volcanic arc are separated into relatively mafic and silicic groups to the west and east, respectively, along a boundary west of Westadahl volcano ($\sim 165^\circ\text{W}$) [Miller *et al.*, 1998]. This boundary corresponds to the transition from the continental to oceanic crustal basement of the arc [House and Jacob, 1983]. Umnak island is part of the mafic group and is located in the central portion of the Aleutian arc (Figure 1). The oblique plate convergence rate in this region is about 67 mm/yr [Cross and Freymueller, 2008; Lallement and Oldow, 2000]. Umnak island comprises two volcanic lobes aligned northeast-southwest and separated by an isthmus. Vsevidof and Recheshnoi, both stratovolcanoes, occupy Umnak southwest of the isthmus. Okmok volcano occupies the island northeast of the isthmus and is one of the largest volcanic shields of the Aleutian arc [Burgisser, 2005]. In spite of its remote location, the relatively active Okmok volcano lies beneath the heavily used north Pacific air traffic corridors and thus an understanding of Okmok's magmatic storage and migration system has significant societal implications [Begét *et al.*, 2005; Larsen *et al.*, 2009]. Over the past decade, Okmok has been instrumented with campaign-style GPS [Fournier *et al.*, 2009; Miyagi *et al.*, 2004] and a local seismic network run by the Alaska Volcano Observatory (AVO), U.S. Geological Survey. However, because of its relatively remote location, the bulk of geophysical observations for Okmok volcano are derived from remote sensing data [Dehn *et al.*, 2000; Lu *et al.*, 2003a, 2005; Patrick *et al.*, 2003].

[5] The geologic history of Okmok is summarized by others [Begét *et al.*, 2005; Miller *et al.*, 1998; Kienle and Nye, 1990; Larsen *et al.*, 2007], and a brief synopsis relevant to our study is presented here. Construction of the volcano began in the late Tertiary and radiometric dating of lava flows indicates eruption activity began about one million years ago [Miller *et al.*, 1998]. The volcanic pile, built on oceanic crust, is dominated by basaltic lava flows, but includes pyroclastic flow deposits to a lesser extent. Detailed records of volcanic activity for Okmok are only available for the past 12,000 years because materials from Pleistocene eruptions are largely buried or were removed by glacial erosion [Begét *et al.*, 2005].

[6] The current physiography of Okmok volcano is dominated by a roughly circular central caldera having a radius of about 5 km (Figure 1b). The maximum elevation of Okmok is 1268 m above msl and is located on Tulik volcano, a parasitic cone on the southeast flank of Okmok. The elevation of the rim of Okmok's caldera is about 900 m, and the elevation of the caldera floor (with the exception of the postcaldera eruption cones) is about 400 m. The caldera

Table 1. InSAR Data Specifications

	Specifications
SAR image pairs	
Image 1	ERS-1 satellite, orbit 22,147, acquired 9 Oct 1995
Image 2	ERS-2 satellite, orbit 12,494, acquired 9 Sep 1997
InSAR data	
Wavelength	C band, 0.0283 cm
Track	115
Pass	descending
Baseline	8 m
LOS [east, north, up]	[0.346, -0.081, 0.935]
Columns	1100
Rows	980
Pixel size	30 m
Reference position (top left corner of image)	UTM zone 2, north 5940915 m, east 670080 m

is the net result of two separate caldera-forming eruptions having ages of about 12,000 and 2050 years, respectively, on the basis of radiogenic measurements [Finney *et al.*, 2008; Larsen *et al.*, 2007]. These two events are somewhat isolated departures from the standard basaltic effusive eruption style of Okmok volcano during postcaldera eruptions, which emanated from intracaldera cones [Burgisser, 2005]. Although the most recent eruption in 2008 originated from several new craters near Cone D, the three previous eruptions in 1945, 1958, and 1997 originated from Cone A [Larsen *et al.*, 2009] (Figure 1b). Geochemical analyses of erupted materials suggest a magma supply from depth having relatively short residence times in shallow reservoirs [Finney *et al.*, 2008].

[7] The 1997 eruption, the subject of this study, began 11 February, on the basis of sightings of steam and ash plumes observed by pilots. Within a few days, Cone A was observed as the source of a moderate strombolian eruption producing explosive ash plumes and lava flows [Miller *et al.*, 1998]. AVHRR imagery revealed thermal anomalies for Okmok caldera during February and March, 1997 [Dehn *et al.*, 2000; Patrick *et al.*, 2003]. The eruption activity continued for several months and ended 23 May 1997 [McGimsey and Wallace, 1999]. Interferometric synthetic aperture radar (InSAR) measurements suggest the resulting lava flows from the 1997 eruption have a net volume of about 0.1 km³ and a maximum thickness of 50 m [Lu *et al.*, 2003a]. InSAR data span the 1997 eruption and map the volcano-wide line-of-sight (LOS) deformation of Okmok. A discussion of the InSAR data processing is presented in Lu *et al.* [2005, and references therein], and the relevant specifications are summarized in Table 1. The unwrapped InSAR data are shown in Figure 1b. The deformation pattern is strongly symmetric about a vertical axis roughly centered on the caldera. The negative LOS displacement (reckoned positive toward the satellite) everywhere on the image suggests volcano-wide deflation, having a maximum LOS displacement of about -1.4 m near the center of the caldera.

[8] The observed deformation spanning the 1997 eruption of Okmok volcano may be caused by several regional and local tectonic processes that fall into three categories. First, convergence of the Pacific and North American

plates produces regional scale strain accumulation having a magnitude of a few centimeters per year and a trench-normal wavelength of a few hundred kilometers [Savage, 1983]. We implicitly neglect this contribution to deformation because of the relatively small spatial and temporal scales involved with the coeruption deformation. At the scale of Okmok volcano, the deformation pattern due to strain accumulation would appear as a plane shift. As discussed later, we estimate plane shift coefficients and remove any volcano-wide plane deformation patterns as part of the parameter optimization to correct for orbital errors embedded in the InSAR image. Second, the emplacement of the extruded lava deforms the caldera floor through a combination of gravity loading and transient poroelastic, thermoelastic, and consolidation processes [Briole *et al.*, 1997; Lu *et al.*, 2005; Masterlark *et al.*, 2006; Patrick *et al.*, 2004; Stevens *et al.*, 2001]. Unfortunately, the InSAR data are largely incoherent for the lava flows extruded during the 1997 eruption of Okmok [Lu *et al.*, 2005], and we cannot resolve the deformation of the lava flows associated with these processes. Third, the change in magma storage depressurizes the magma reservoir as magmatic mass migrates out of the reservoir and is extruded at the land surface. This decrease in pressure causes a relatively rapid volcano-wide deflation pattern, with its greatest magnitude roughly centered above the reservoir [Mogi, 1958]. The deformation pattern is not precisely centered above the magma reservoir because the LOS vector includes nonzero horizontal components (Table 1). Because the InSAR-observed deformation pattern is overwhelmingly dominated by this third category, we focus our modeling efforts on the coeruption mass flux from the magma reservoir and the associated rheologic and structural controls on the resulting volcano-wide deformation.

[9] Surface deformation and seismic waves are linked through their dependence on elastic properties, and therefore a joint study of the two fields provides greater constraints on the subsurface structure at Okmok. A standard technique for studying volcanic structure in seismology, known as local earthquake tomography (LET), relies on an existing catalog of earthquake phase arrivals from a seismic network. Such catalogs require many years of observations and depend on the occurrence of seismicity which has clear, well-defined onsets (e.g., tectonic or volcano-tectonic earthquakes). At Okmok, neither of these conditions prevails: the seismic network, operated by the AVO, has only been in place since 2002 and much of the seismicity has an emergent character (e.g., volcanic tremor). As a result, the catalog from 2002 to 2007 has only ~200 phase arrivals, a number much smaller than catalogs used for LET at nearby volcanoes [Jolly *et al.*, 2007]. Because of the remote location and lack of a long-term seismic network, there are only two previous publications on the local seismicity at Okmok [Byers *et al.*, 1947; Caplan-Auerbach *et al.*, 2004], although another regional study deployed temporary seismometers on Umnak Island [Fliedner and Klempner, 1999].

[10] An alternative to LET is the emerging technique known as ambient noise tomography (ANT). Ambient noise has recently been recognized as a usable type of signal in seismology. Applications have followed in tomography

[Shapiro et al., 2005; Gerstoft et al., 2006; Bensen et al., 2007; Brenguier et al., 2007], seismic hazard analysis [Prieto and Beroza, 2008], and temporal monitoring [Brenguier et al., 2008a, 2008b]. The fundamental principles of ambient noise seismology originate in pioneering work by Aki [1957, 1965] and by Claerbout [1968]. The method exploits the fact that the cross correlation of seismic noise recordings at two different stations reproduces the Green's function as if one of the stations were a source and the other a receiver. Thus, passive noise data can be synthesized into virtual active source data. Lacking a substantial catalog at Okmok for LET, we pursue ANT to image the subsurface structure of the volcano. As in other studies [Shapiro et al., 2005; Gerstoft et al., 2006; Bensen et al., 2007; Brenguier et al., 2007], we depend on the oceanic microseism as the source of the ambient noise. The microseism arises because of the coupling of ocean waves and the solid Earth. In general, this noise exists for frequencies below 1 Hz and is strongest at the so-called single and double frequency peaks around 0.07 and 0.14 Hz [Gerstoft et al., 2006]. Okmok is well suited for ANT because Umnak island is located between the Pacific Ocean and the Bering Sea and plenty of ocean noise streams across the network, in particular during the northern winter months.

[11] Previous studies precisely estimate the deformation source parameters and predict the coeruption InSAR data remarkably well [Lu et al., 2000, 2005; Mann et al., 2002]. However, none of these studies accounts for the material property distribution required by the new tomography results presented in this study and as a result, underestimate the depth of the magma reservoir. The material property distributions previously suggested by Masterlark [2007], include a shallow layer of weak materials covering the caldera floor, which consequently leads to deeper magma reservoir depth estimations that agree with the new tomography data. In addition to discrepancies between simulated and actual distributions of material properties, the magnitudes of depressurization estimated for many previous studies severely exceed lithostatic limits.

[12] The aim of this study is to simulate the coeruption deformation system of Okmok volcano, due to magma migration from a shallow reservoir and extrusion onto the caldera floor. The deformation model predicts the InSAR data, while simultaneously accounting for the seismic velocity distribution from new tomography data and temperature-dependent rheologic properties that satisfy lithostatic constraints on the deformation source. The remainder of this paper is organized into four sections. First, the main body of the paper describes the ambient noise tomography and the design, construction, and implementation of thermal and deformation models, the latter of which are driven by magma mass extraction from a relatively shallow magma reservoir. We then present the results, which describe the selection of optimal calibration parameters and residual assessments. This is followed by a discussion of the deformation model as an impulse-response system driven by magma storage and migration. We then discuss the roles of structural, rheologic, and lithostatic controls on magma migration from a reservoir at depth (beneath the center of the caldera) to lava extrusion at

the caldera margins. Finally, we present conclusions and recommendations.

2. Method

[13] A suitable model of this coupled eruption and deformation system must (1) quantitatively predict the coeruption InSAR data, based on coeruptive mass flux from a magma reservoir; (2) account for the distribution of elastic material properties indicated by the tomography; and (3) include a realistic rheologic distribution that results in reservoir depressurization values that satisfy lithostatic constraints while maintaining the required magnitudes of the observed surface deformation.

[14] The concept of rheologic partitioning is based on the expected thermomechanical weakening of surrounding rocks by the magma reservoir [Dobran, 2001]. *Dragoni and Magnanensi* [1989] provide analytical solutions for the displacement and stress for a pressurized sphere, surrounded by a linear (Maxwell) viscoelastic shell, embedded in a homogeneous, elastic, full-space. These solutions predict, for example, deformation observed for Campi Flegrei volcano, Italy, that require a magma reservoir pressure that is an order of magnitude lower than that required for a fully elastic problem domain [Mogi, 1958]. However, a severe limitation of the solutions presented by *Dragoni and Magnanensi* [1989] is that they are valid for a full-space problem domain and do not account for a stress-free surface, corresponding to the land surface of a volcano. To account for a free surface, *Newman et al.* [2001, 2006] demonstrated that FEMs can readily simulate surface deformation due to the pressurization of spherical and elliptical chamber-like magma reservoirs that are surrounded by viscoelastic rinds. Results of these analyses again demonstrate that the viscoelastic rinds greatly reduced the magnitude of pressurization required to simulate surface deformation, compared to fully elastic half-space models. *Del Negro et al.* [2009] took this approach a step further by simulating a pressurized sphere embedded in an entirely viscoelastic problem domain, having a temperature-dependent viscosity structure constrained by thermal models. Like the viscoelastic rind models, the purely viscoelastic model configuration predicts the magnitude of deformation similar to fully elastic models, but requires a substantially lower pressure load along the walls of the embedded spherical cavity.

[15] We construct a series of FEMs to initially simulate the thermal regime that constrains the spatial characteristics of the rheologic configuration and subsequently simulate deformation for a suite of model configurations that include the distribution of rheologic properties indicated by the new tomography data. The deformation FEMs are driven by mass flux, q , into a magma reservoir surrounded by a viscoelastic rind having a viscosity of μ . We construct all FEMs in this study with the general purpose FEM code Abaqus (<http://www.simulia.com>) and sweep through $\mu - q$, parameter space to find the optimal (calibrated) pair of parameters in terms of predicted versus observed deformation. Model specifications are given in Table 2.

[16] We take advantage of the radial symmetry of the caldera structure, the InSAR deformation pattern, and the tomography results and simulate an axisymmetric problem domain. The axis of symmetry is normal to the land surface

Table 2. Model Configurations and Parameters

Parameter	Description	References
<i>Analytical Model [Mogi, 1958]</i>		
Deformation model		
Problem domain	Axisymmetric, homogeneous, elastic, half-space	
Diabase	$G = 3.0 \times 10^{10}$ Pa $\nu = 0.25$	<i>Turcotte and Schubert [2002]</i> <i>Mogi [1958]</i>
Magma reservoir effective radius	$r_s = 1000$ m	<i>Masterlark [2007]</i>
<i>FEMs</i>		
Common specifications		
Problem domain geometry	Axisymmetry	
Magma reservoir depth	5000 m	
Magma reservoir radius	1500 m	
Moho depth	30 km	<i>Fliedner and Klemperer [1999]</i>
Lateral extent	50 km	
Thermal model		
Brittle-plastic transition	750°C	<i>Hirth [1998]</i>
Magma reservoir solidus (1 GPa)	1200°C	<i>Winter [2001]</i>
Moho	600°C	<i>Stern [2002] and Winter [2001]</i>
Deformation model		
Diabase	$\rho = 2936$ kg/m ³ $\nu = 0.277$ $G = 3.0 \times 10^{10}$ Pa ($E = 7.662 \times 10^{10}$ Pa) $V_s = 3.2$ km/s	<i>Christensen [1996]</i> <i>Christensen [1996]</i> <i>Turcotte and Schubert [2002]</i>
Weak caldera	$\rho = 1800$ kg/m ³ $\nu = 0.15$ $G = 3.478 \times 10^9$ Pa ($E = 8.0 \times 10^9$ Pa) $V_s = 1.39$ km/s	
Mantle	$\nu = 0.28$ $G = 6.82 \times 10^{10}$ Pa ($E = 1.7459 \times 10^{11}$ Pa)	<i>Turcotte and Schubert [2002]</i> <i>Turcotte and Schubert [2002]</i>
Validation model		
Magma reservoir depth	5000 m	
Magma reservoir radius	$r_s = 1500$ m	
Shear modulus	$G = 4.0 \times 10^9$ Pa	
Poisson's ratio	$\nu = 0.25$	
Pressure	$\Delta P = 10$ GPa	

and roughly centered on the caldera. Previous studies also used this symmetry to successfully predict preeruption, coeruption, and posteruption InSAR and GPS data [Fournier et al., 2009; Lu et al., 2000, 2005, Mann et al., 2002; Masterlark, 2007; Miyagi et al., 2004]. A full 3-D problem domain is recovered by rotating predictions about the axis of symmetry. This axisymmetric deformation field is translated to the positions of the coherent InSAR data pixels, a requirement for predicting the LOS deformation of the InSAR data, by Delaunay triangulation and bilinear interpolation. As demonstrated in previous studies [Lu et al., 2000, 2005, Mann et al., 2002; Masterlark, 2007], the high signal-to-noise ratio and strong radial symmetry of the deformation pattern is compatible with a simple Mogi [1958] deformation model, which allows us to precisely and efficiently estimate the position of the axis of symmetry as an a priori constraint for the FEMs. The forward solution for displacement, u , at point j on the free surface, caused by a spherical expansion source embedded in a homogeneous, isotropic, elastic half-space, is

$$u_j = s u_j^*, \quad \text{and} \quad u_j^* = [(x - \xi_x), (y - \xi_y), (-\xi_z)]/R^3, \quad (1)$$

where s is the source strength; ξ is the central position of the spherical expansion source; R is the Euclidean distance from ξ to j ; x , y , and z are Cartesian coordinates; and z is orthogonal to the free surface and upward positive [Masterlark, 2007]. The predicted displacement is a linear function of

s , which can be expressed in terms of either a change in volume, ΔV , of the embedded sphere or a change of pressure, ΔP , along the surface of the sphere

$$s = \Delta P(1 - \nu) \frac{r_s^3}{G} = \Delta V \frac{(1 - \nu)(1 + \nu)}{2\pi(1 - 2\nu)} \quad \text{and} \quad \Delta P = K \frac{\Delta V}{V}, \quad (2)$$

where ν is Poisson's ratio, r_s is the radius of the sphere, G is the shear modulus, K is the bulk modulus, and V is the volume of the sphere [Dobran, 2001; McCann and Wilts, 1951; Turcotte and Schubert, 2002]. The Mogi [1958] equations are recovered by recasting (1) into a radial coordinate system and substituting $\nu = 0.25$ in (2). The predicted displacement is a nonlinear function of the position of the source with respect to a given point j on the free surface. These equations, (1) and (2), are embedded in Monte Carlo simulations of the downhill simplex method [Press et al., 2007] to estimate the position of the axis of symmetry (x_0, y_0), the depth and strength of the source, and plane shift coefficients to allow for uncertainties in the orbital positions [Massonnet and Feigl, 1998]. This estimation minimizes the L_2 norm, $\|\mathbf{d}_{\text{obs}} - \mathbf{d}_{\text{pre}}\|_2^2$, where \mathbf{d}_{obs} and \mathbf{d}_{pre} are the observed and predicted data vectors, respectively [Aster et al., 2005]. Parameters and specifications for this analysis are summarized in Table 2. Parameter correlation matrices are not diagonal for estimations of position couples for the horizontal location of the axis of

symmetry (S_{xy}), as well as for source depth and pressure couples (S_{pd}). Results of this analysis are shown in Figure 2 and summarized in Table 3.

2.1. Ambient Noise Tomography

[17] We analyze 40 days of continuous seismic data in late 2005 at Okmok to image the subsurface structure of the volcano. We select these 40 days on the basis of the Okmok network being in the best overall condition during that time. Previous studies [Shapiro *et al.*, 2005; Ma *et al.*, 2008] have demonstrated that one month may be a sufficient time period to reliably estimate the impulse response. In any case, the reliability of the impulse response can be estimated for different locations and frequencies by consideration of the signal-to-noise ratio (SNR), as discussed later. The seismic network at Okmok volcano is one of the most extensive in the Aleutian Arc and it motivates the application of ANT. In late 2005, the network consisted of 12 functioning seismic stations: 9 vertical component short period instruments and 3 three-component broadband

instruments (Figure 3 and Table 4). An additional broadband instrument on the southeast side of Okmok was not operating at the time. The short period instruments at Okmok are L4 seismometers with a natural period of 1 Hz; the broadband seismometers are CMG-6TD with a natural frequency of 0.033 Hz (30 s period) and a high corner frequency of 50 Hz.

[18] A challenge for our study concerned the use of the two types of instruments. Previous ANT studies [Gerstoft *et al.*, 2006; Brenguier *et al.*, 2007] used networks made up of a single type of seismometer, either broadband or short period. The use of both short period and broadband seismometers demanded the issue of instrument responses be addressed since an unaccounted difference in the phase spectrum of two instruments would lead to delay times which are not entirely related to propagation. We adopted the following approach to the issue. Instead of deconvolving the responses of each instrument, a process that is sensitive to electronic noise (e.g., spikes), we elected to reduce all the instruments to a standard seismometer. Such an instrument simulation [Scherbaum, 1996] is more robust because the inverse filter does not become unbounded at low frequencies and achieves the goal of a uniform phase and amplitude response across the network. For the standard seismometer, we chose an underdamped short period L4 seismometer with a damping coefficient [Scherbaum, 1996] of 0.67. Because there are two instances of colocated broadband and short period seismometers in the network operated by AVO, we were able to uniquely check our instrument correction. These colocated instruments are part of the AVO networks at Mount Spurr and Augustine volcanoes. Such deployments, though seemingly inefficient, attest to the rough terrain and limited number of acceptable sites on Alaskan volcanoes.

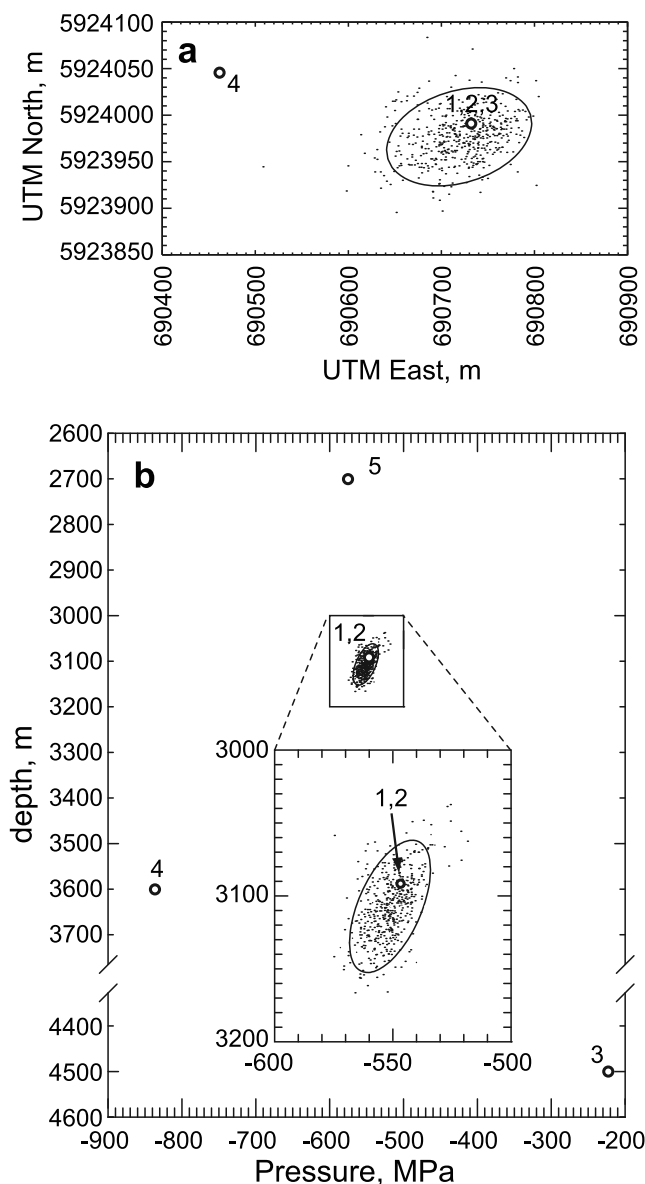


Figure 2. Analytical solution results. We estimate suites of parameters that minimize misfit for 500 realizations of the InSAR data. Confidence intervals are based on principal component analyses of the parameter correlation matrices [Davis, 2002]. Pressure estimates are computed from reported ΔV estimates using G , ν , and r_s given in Table 2. (a) Horizontal position parameters. Each black dot represents the estimated location of the vertical axis of symmetry (x_0, y_0) that minimizes the L_2 norm for one realization of the InSAR data. The first moment of distribution is our assumed vertical axis of symmetry for subsequent models. The ellipse represents 95% confidence determined from S_{xy} (Table 3). (b) Depth and pressure of the deformation source. Each black dot represents a pair of pressure and depth parameters that minimize the L_2 norm for one realization of the InSAR data. The ellipse represents 95% confidence determined from S_{pd} (Table 3). Note the break in the depth axis. The inset shows details of the distribution. Corresponding parameter estimations from previous analyses are indicated by numbers as follows: 1, Lu *et al.* [2005]; 2, Masterlark [2007] (Model A); 3, Masterlark [2007] (Model H); 4, Mann *et al.* [2002]; 5, Lu *et al.* [2000] (horizontal position not reported). The depth for Masterlark [2007] (Model H) is much deeper than the other estimates, because it is based on an FEM that includes a heterogeneous distribution of material properties, similar to that suggested by the tomography presented in this study.

Table 3. Analytical and Numerical Modeling Results^a

Parameter	Description
<i>Analytical Model</i>	
UTM east (x_0), m	690719
UTM north (y_0), m	5923980
Depth, m	3110
Pressure, MPa	-551
L_2 norm, m^2	13.8
<i>FEMs</i>	
Elastic only	
Flux, kg/d	$q_e = -4.4 \times 10^9$
Pressure, MPa	-244
L_2 norm, m^2	64.0
Viscoelastic rind	
Flux, kg/d	$q_e = -4.2 \times 10^9$
Peak pressure, MPa	-121
Residual pressure, MPa	-68
Viscosity, Pa s	7.5×10^{16}
L_2 norm, m^2	44.7

$${}^a \mathbf{S}_{xy} = \begin{bmatrix} \text{var } x & \text{cov } yx \\ \text{cov } xy & \text{var } y \end{bmatrix} = \begin{bmatrix} 1520.1 & 285.20 \\ 285.20 & 696.22 \end{bmatrix}$$

$$\text{and } \mathbf{S}_{Pd} = \begin{bmatrix} \text{var } P & \text{cov } dP \\ \text{cov } Pd & \text{var } d \end{bmatrix} = \begin{bmatrix} 73.46 & 107.1 \\ 107.1 & 513.7 \end{bmatrix}.$$

Our tests showed that the instrument responses are well modeled over a broad frequency band, including the frequency band of microseismic ocean noise used in this study from 0.2 to 0.7 Hz.

[19] After compensating for the instrument responses, we process the data according to the typical ANT sequence for a single station [Bensen *et al.*, 2007] with a few minor adjustments. For time normalization, we use a running RMS normalization instead of either a sign bit [Brenquiere *et al.*, 2007] or a running absolute mean normalization [Bensen *et al.*, 2007]. The RMS normalization multiplies each time sample, d , by a weighting factor, W , given by

$$W_n = \sqrt{\frac{1}{(2N+1)} \sum_{m=n-N}^{n+N} d_m^2}, \quad (3)$$

where $(2N+1)$ is the window length in samples. Similar to the findings of Bensen *et al.* [2007] regarding the running absolute mean normalization, we find the running RMS normalization to be superior to the sign bit normalization. A running RMS normalization is better known as automatic gain control (AGC) in seismic data processing [Yilmaz, 1987]. We set the length of the time window for the AGC to 10 s, or twice the maximum period considered for the impulse responses. We find that the results do not depend strongly on the exact value of the window length, in agreement with the observations of Bensen *et al.* [2007] for the running absolute mean normalization. Both the AGC and the running absolute mean normalization can be seen as generalized versions of sign bit normalization, since setting the window length to a single sample for either technique results in a scaled version of the sign bit normalization. Following the time normalization, we whiten the signal over the frequency band of interest, from 0.2 to 0.7 Hz. Following the AGC and whitening step, we cross correlate hour-long signals between all channels and stack to obtain the result for a single day. We visually inspect some of the daily cross correlations over the 40 days from individual

stations to ensure quality control. Figure 4 shows 40 daily cross correlations between channels OKSP and OKCEr (radial component) in the frequency bands 0.3 and 0.5 Hz. The correlations are seen to be highly repeatable from day to day. The final cross correlation used for ANT is the stack of all the daily cross correlations over the 40 day period.

[20] To maximize the available data, we use the radial components from the three broadband at Okmok. Together with the vertical components from the 12 seismometers, this yields 15 data channels available for cross correlation. We select the radial component between station pairs because we are interested in the fundamental mode Rayleigh wave, which is limited to the vertical and radial components.

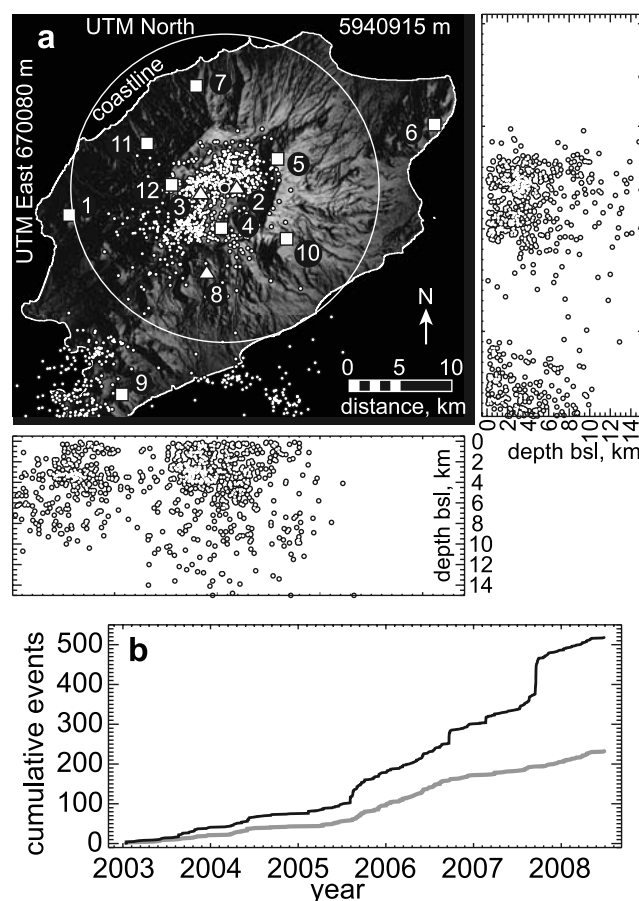


Figure 3. Seismic network and seismicity. (a) The seismic network at Okmok volcano (late 2005) consists of nine short period vertical stations (squares) and three broadband three-component stations (triangles). Station names are summarized in Table 4. The large black circle near the center of the caldera is the best fit horizontal position (vertical axis of symmetry) of the deformation source, as shown in Figure 2. Small white circles outlined in black represent seismicity spanning 2003–2008. [Dixon *et al.*, 2003, 2004, 2005, 2006, 2008a, 2008b]. (b) Cumulative seismicity. Black curve represents all events shown in Figure 3a. Gray curve represents events local to Okmok caldera (within the large white circle shown in Figure 3a). There is no clear temporal correlation between inferred pulses of magma [Fournier *et al.*, 2009] and seismicity local to the caldera.

Table 4. Okmok Seismic Network, 2005

Station	Name	Longitude (°W)	Latitude (°N)	UTM East ^a (m)	UTM North ^a (m)
1	OKAK ^b	-168.35776	53.412334	675,610	5,921,393
2	OKCD ^c	-168.11229	53.430302	691,840	5,924,024
3	OKCE ^c	-168.16431	53.427032	688,399	5,923,522
4	OKCF ^b	-168.13625	53.395817	690,403	5,920,125
5	OKER ^b	-168.04933	53.454632	695,909	5,926,901
6	OKID ^b	-167.81619	53.477417	711,270	5,930,101
7	OKRE ^b	-168.16409	53.520248	688,001	5,933,889
8	OKSO ^c	-168.15985	53.357449	689,003	5,915,795
9	OKSP ^b	-168.29051	53.252602	680,753	5,903,797
10	OKTU ^b	-168.04111	53.383915	696,781	5,919,059
11	OKWE ^b	-168.23981	53.472134	683,190	5,928,341
12	OKWR ^b	-168.20555	53.434734	685,626	5,924,270

^aUTM zone 2.^bShort period vertical station.^cBroadband three-component station.

Although in theory the group velocity (arrival time of the envelope of the waveform) estimated from the radial component should be exactly the same as from the vertical component, we find that including the radial component offers another measurement for use in ANT. For a single broadband station, we apply the same AGC and whitening filters to each of the three components to maintain balance between the components, in a way similar to that described by *Lin et al.* [2008] for horizontal components. We always use the vertical component to define the AGC and whitening filters. The radial component is found by simply rotating the horizontal components for a particular station pair. With 15 data channels, there are possibly as many as 102 ($=15 \times 14/2 - 3$) different pairs available for ANT. Note that the three correlations between vertical and radial components for the same broadband are not used.

[21] For a station pair, the calculation of a group velocity dispersion curve begins by forming the symmetric component from the two-sided cross correlation [*Bensen et al.*, 2007]. This is followed by applying a sequence of narrow-band Gaussian filters to the analytic signal of the symmetric component [*Bensen et al.*, 2007]. This gives the amplitude of the envelope of the narrowband data as a function of time

and frequency. By mapping the time axis into a velocity axis (since source-receiver distance is known), an “energy diagram” [*Romanowicz*, 2002] is formed where the group velocity dispersion curve can be picked at the maximum (Figure 4c). We sample these dispersion curves at intervals of 0.01 Hz. We reject obtained group velocities, or group traveltimes, on the basis of similar criteria as given by *Gerstoft et al.* [2006]: we set lower and upper bounds on acceptable group velocities (0.5 and 5.0 km/s), specify a minimum signal-to-noise ratio of 5, and we only accept group traveltimes when the receivers are separated by at least one wavelength as described by *Brenguier et al.* [2007]. Since we consider the frequency band from 0.2 to 0.7 Hz, in contrast to the band from 0.05 to 0.2 Hz as given by *Gerstoft et al.* [2006], we define the time window for our noise estimate to have a length of 10 s, extending from 40 to 50 s time. This results in between 55 and 85 channel pairs out of a possible 102 pairs being retained over the frequency band from 0.2 to 0.7 Hz. The envelopes of the correlations at 0.3 Hz display generally increasing times for their maximum as a function of receiver-receiver distance, as is expected (Figure 5). The deviations from a purely linear trend bear the imprint of the 3-D structure we seek to image.

[22] We perform group velocity tomography on each frequency from 0.2 to 0.7 Hz at intervals of 0.01 Hz. We choose an upper frequency of 0.7 Hz since the oceanic microseismic signal becomes weak for higher frequencies at Okmok; we select a lower threshold of 0.2 Hz as given by *Brenguier et al.* [2007]. Our initial model for Okmok is a 1-D layered model as shown in Table 5. As a result, our initial models for group velocity tomography are laterally homogeneous. We use the program VELEST [*Kissling et al.*, 1994] to construct the initial layered model of seismic velocities from the limited catalog (<200 earthquakes) available at Okmok. Thus, even though we use ambient noise to construct a 3-D model, earthquake data are indispensable for forming the initial layered model. We smooth the 1-D layered velocity model from VELEST over a depth range of 1 km to compute Rayleigh wave group velocities for each frequency. We forward model the Rayleigh waves using the FEM of *Lysmer* [1970]. Given a frequency, ω , this method

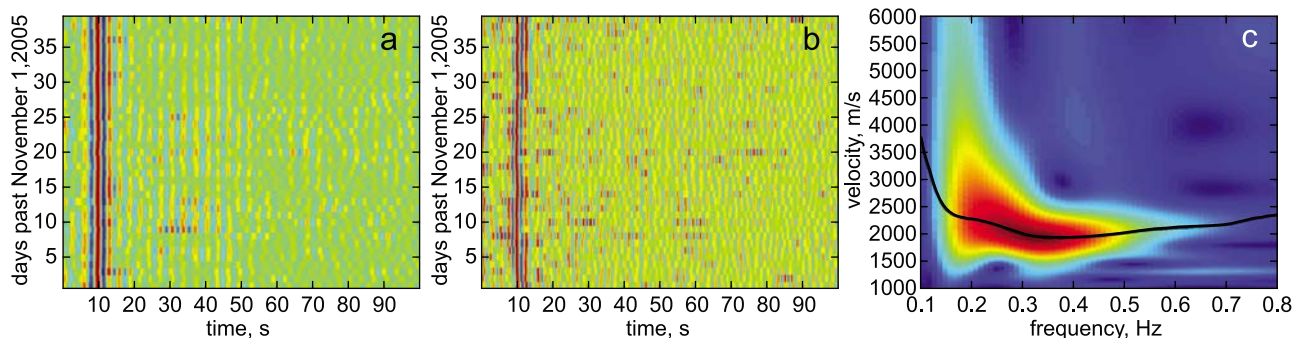


Figure 4. Daily correlations between channels OKSP and OKCEr (radial component) for 40 days in late 2005 in two frequency bands, (a) 0.3 Hz and (b) 0.5 Hz. The correlations are seen to be highly repeatable from day to day. The final correlation is the stack of these 40 daily correlations. (c) The dispersion curve represents the amplitude of the fundamental Rayleigh wave between these stations. The peak amplitude, at 0.3 Hz, results from a tradeoff between the strength of the ocean noise (increases with decreasing frequency) and the instrument response of the standard seismometer (decreases with decreasing frequency).

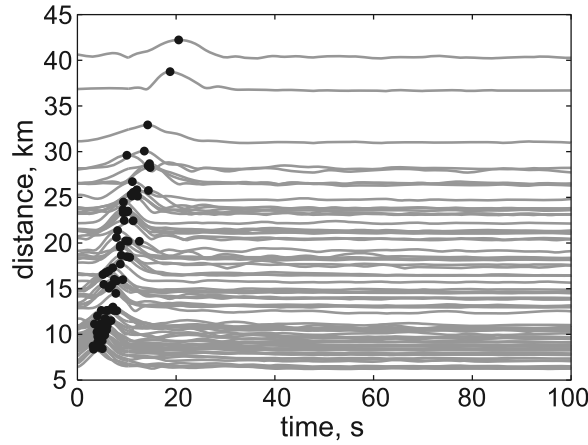


Figure 5. The envelopes for all qualifying channel pairs at 0.3 Hz on the Okmok network plotted as a function of station-station distance (gray curves). The peaks of the envelopes (black circles) move out with distance with increasing time.

poses the forward modeling as an eigenvalue/eigenvector problem

$$\mathbf{B}_w \mathbf{v} = \omega^2 \mathbf{M} \mathbf{v} \quad \text{and} \quad \mathbf{B}_w = (w^2 \mathbf{B}_2 + w \mathbf{B}_1 + \mathbf{B}_0), \quad (4)$$

where \mathbf{B}_2 , \mathbf{B}_1 , \mathbf{B}_0 , and \mathbf{M} are matrices dependent on elastic properties and density given by *Lysmer* [1970], w is the wave number of the Rayleigh wave, and \mathbf{v} is the eigenvector describing the depth dependence of the Rayleigh wave mode shape. We solve (4), a generalized quadratic eigenvalue problem, in terms of the wave number using the ARPACK eigensolver in Matlab. Once the eigenvector and eigenvalue are calculated, the group velocity, V_g , is given by

$$V_g = \frac{\mathbf{v}^T (2w \mathbf{B}_2 + \mathbf{B}_1) \mathbf{v}}{2\omega \mathbf{v}^T \mathbf{M} \mathbf{v}}, \quad (5)$$

where the superscript T denotes the matrix transpose operator. The group velocities calculated in this manner define the laterally homogeneous starting models at each frequency for the 2-D surface wave tomography. We use a 2-D ray-based tomography code by *Aldridge and Oldenburg* [1993], originally developed for 2-D cross-well tomography, to do the group velocity tomography at each frequency. Although the code is able to model ray bending, we use straight rays for the group velocity tomography as given by *Gerstoft et al.* [2006]. Straight rays are necessary since we perform group velocity tomography and phase velocities, which cannot be obtained from group velocities [*Bensen et al.*, 2007], are needed to calculate ray bending. Because the code is written for Cartesian coordinates, we use the coordinate approximations defined by *Richter* [1943] which are accurate to distances of 500 km. The numerical grid for the tomography is made up of 20×28 cells in the east-west and north-south directions, respectively, with each cell being $2.25 \times 2.25 \text{ km}^2$. We apply strong smoothing constraints to the inverted group velocity maps and from checkerboard tests (Figure 6) to judge that we are able to laterally recover

gross features on the length scale of 8 km within the caldera at Okmok. The group velocity tomography reduces the RMS error by 25% on average over the entire frequency from 0.2 to 0.7 Hz. From the tomography map of Rayleigh wave group velocity at 0.3 Hz, it is clear that the caldera is locally a low-velocity zone (LVZ, Figure 7). The LVZ is close to the lateral position of the deformation source inferred by *Lu et al.* [2005] and *Mann et al.* [2002], on the basis of InSAR data.

[23] With the tomography complete, we have group velocity as a function of position and frequency at Okmok. The final step inverts the local dispersion curves (group velocity versus frequency curves) at each horizontal position for a depth model. Applying the inversion at all lateral coordinates gives a 3-D model. For the forward problem defined by (4), a perturbation in the Rayleigh wave phase velocity due to a small change in shear or compressional wave velocity or density can be written as

$$\frac{\delta c}{c} = \frac{1}{2w^2 V_g c \mathbf{v}^T \mathbf{M} \mathbf{v}} \times \left(\sum_{m=1}^M \mathbf{v}^T \frac{\partial \mathbf{B}_w}{\partial V_{p(m)}} \mathbf{v} \delta V_{p(m)} + \sum_{m=1}^M \mathbf{v}^T \frac{\partial \mathbf{B}_w}{\partial V_{s(m)}} \mathbf{v} \delta V_{s(m)} - \omega^2 \sum_{m=1}^M \mathbf{v}^T \frac{\partial \mathbf{M}}{\partial \rho_m} \mathbf{v} \delta \rho_m \right), \quad (6)$$

where $c = \omega/w$ is the phase velocity, V_s is shear wave velocity, V_p is compressional wave velocity, ρ is density, and the model is discretized into M elements using the method of *Lysmer* [1970]. This expression, (6), is the discrete analog of the continuous relation shown by *Aki and Richards* [1980]. As is common in Rayleigh wave inversions, we attempt to decrease the nonuniqueness of the solution by adopting relationships between V_p and V_s as well as ρ and V_s . We take $V_p/V_s = 1.78$ and assume Gardner's relation for density, as has been employed in a previous application of Rayleigh wave inversion at Kilauea volcano [*Saccorotti et al.*, 2003]. As a result, perturbations in V_p and V_s can be related to perturbations in V_s and the depth model is defined only in terms of V_s . By imposing these relations and evaluating (6) at many frequencies, the linear matrix relation becomes

$$\frac{\delta c}{c} = \mathbf{K}_c \frac{\delta V_s}{V_s}, \quad (7)$$

Table 5. Initial Seismic Velocity Model for Surface Wave Tomography and Depth Inversion

Layer	V_p^a (km/s)	Depth of Layer Top (km)
1	3.83	Surface
2	3.89	0
3	5.08	1
4	5.19	2
5	5.47	3
6	6.18	4
7	6.19	10
8	6.45	12
9	6.90	15
10	7.41	20
11	7.70	25
12	7.90	33
13	8.10	47
14	8.30	66

^a $V_p/V_s = 1.78$.

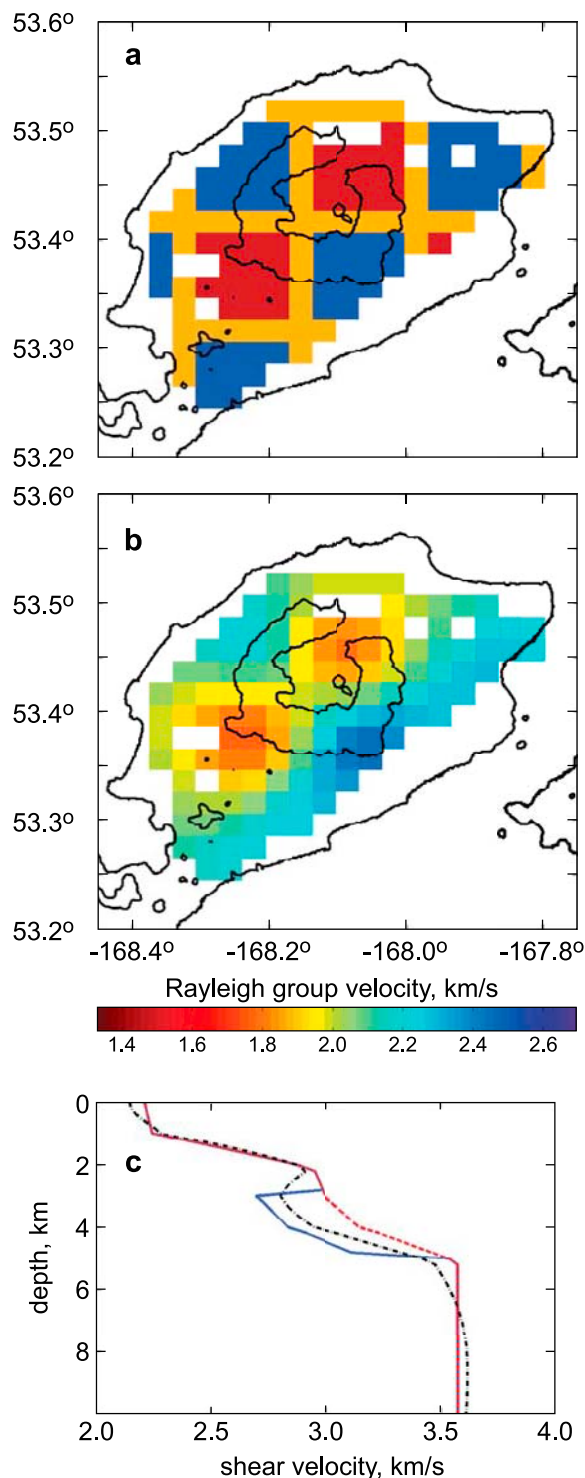


Figure 6. Resolution. A checkerboard test for tomographic resolution at 0.3 Hz: (a) the input checkerboard and (b) the tomographic result using the same damping parameters as used in this study. (c) Resolution test for the surface wave depth inversion step. The true model (blue) is the same as the Okmok layered model (Table 5) except that it has 20% lower velocity between the depths of 3 and 5 km. Using the Okmok layered model as the initial guess (red), the inverted model (black) is seen to recover a smooth version of the true model. This test demonstrates that resolution is acceptable to depths of 5 km at Okmok.

where \mathbf{K}_c is the phase velocity kernel mapping perturbations in shear wave velocity with depth to phase velocity perturbations with frequency. As shown by *Rodi et al.* [1975], the group velocity kernel can be obtained in a straightforward manner from the phase velocity kernel. The group velocity kernel makes it possible to invert group velocities according to

$$\frac{\delta V_g}{V_g} = \mathbf{K}_g \frac{\delta V_s}{V_s}, \quad (8)$$

where \mathbf{K}_g is the group velocity kernel and V_g is the group velocity. Performing this inversion at each longitude and latitude yields a 3-D model of shear wave velocity at Okmok. For the inversion, we use $M = 151$ finite elements each with a depth extent of 200 m. The depth inversion proceeds with an average RMS reduction of 70% over all lateral points. Regularization is introduced to stabilize the inversion by assuming data and model covariances of 10% and a smoothing length of 1 km in depth. From resolution tests of the depth inversion step, we conclude that resolution is acceptable to depths of 5 km, as shown in Figure 6. The resulting ANT 3-D velocity model for Okmok volcano is given in Figure 7.

2.2. Thermal Model

[24] The thermal model simulates the steady state temperature distribution associated with basal heating along the Moho and the thermal contribution from the magma reservoir. Radiogenic heat is negligible for basaltic rocks and in the absence of heat sources, the temperature distribution satisfies Laplace's equation [*Turcotte and Schubert, 2002*]. The specified temperature at the land surface is 0°C. Heat flux is zero along the axis of symmetry and far-field lateral boundary. The Moho temperature is 600°C (depth of 30 km), based on regional scale thermal models of subduction [*Stern, 2002; Winter, 2001*]. The specified temperature within the magma reservoir is 1200°C, the solidus temperature for diabase at 1 GPa [*Winter, 2001*]. Petrologic data for the 1997 Okmok lava flow suggest a minimum temperature of 1015°C [*Izbekov et al., 2005*]. This conceptual configuration is similar to the thermal model proposed for the shallow magma reservoir of Etna volcano [*Del Negro et al., 2009*].

[25] The configuration of the axisymmetric problem domain is shown in Figure 8a. The problem domain is tessellated into 5482 first-order triangular finite elements. The characteristic length of elements is about 100 m near the magma reservoir and increases to about 1000 m at the lateral and basal boundaries. Computation times are negligible on a 64 bit PC capable of solving the entire problem in physical memory. The resulting temperature is the superposition of the geothermal gradient and the temperature perturbation of the magma reservoir (Figure 8b). The 750°C isotherm demarks the brittle-ductile transition for diabase at a depth of 5 km [*Hirth, 1998*], which envelops the viscoelastic rind surrounding the magma reservoir. The rind is approximately spherical with a diameter of 4500 m and a thickness of 750 m. Lowering the brittle-ductile threshold will result in a thicker rind, which will conceptually increase the predicted viscoelastic behavior. For the limiting case of the entire problem domain having a temperature-dependent viscosity, the brittle-ductile transi-

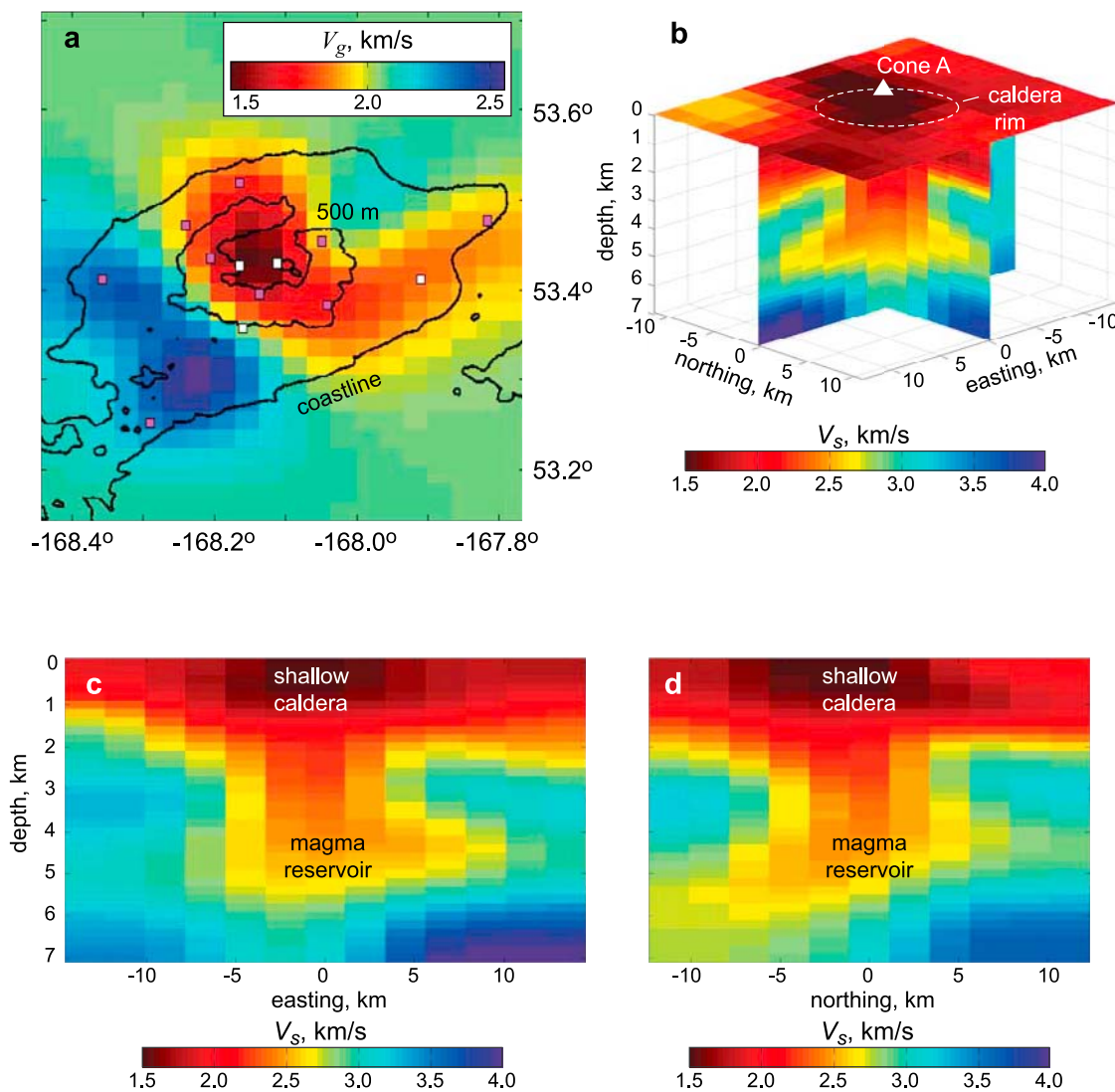


Figure 7. Velocity model. (a) Two-dimensional group velocity tomography at 0.3 Hz. Elevation contours are at 0 and 500 m. The caldera is seen to be a local LVZ with respect to the rest of Umnak Island. Short period and broadband stations are plotted as pink and white squares, respectively. (b) Slices through the 3-D model at Okmok, showing the lateral extent of the shallow LVZ at the top and the northeast side of the deep LVZ. (c) North-south and (d) east-west cross sections through the 3-D model. Two LVZs are evident: one at shallow depths (<2 km) and another at depths greater than 4 km. The shallow LVZ represents weak caldera material. The deep LVZ is indicative of the persistent magma reservoir beneath Okmok.

tion vanishes. *Del Negro et al.* [2009] construct such a model and demonstrate that viscoelastic deformation is insignificant for temperatures less than about 400°C. However, *Hirth et al.* [1998] indicate that temperatures less than 750°C produce effective viscosities greater than 10^{19} Pa s, which we will later show to have an effectively elastic behavior for the Okmok deformational system over the time intervals spanned by the coeruption InSAR data.

2.3. Deformation Models

[26] The deformation models simulate quasi-static displacement due to mass flux from a shallow magma reservoir. The magma reservoir, revealed in the tomography data (Figure 7), is interpreted as a relatively high-density network of magma-filled structures, rather than a single fluid-

filled cavity [*Dobran, 2001; Ryan, 1987a*]. The details of this network at depth cannot be resolved from deformation at the land surface, as described by St. Venant's principle [*Housner and Vreeland, 1966*], and the network is effectively simulated as an isometric body at depth. We construct FEMs to solve for displacements over a problem domain partitioned into elastic and viscoelastic regions. Expressed in index notation, the elastostatic governing equations are

$$G\nabla^2 u_i + \frac{G}{(1-2\nu)} \frac{\partial^2 u_k}{\partial x_i \partial x_k} = -F_i, \quad (9)$$

where G is the shear modulus, ν is Poisson's ratio, and F is a body force per unit volume [*Wang, 2000*]. The subscript i spans orthogonal direction components 1, 2, and 3, and the

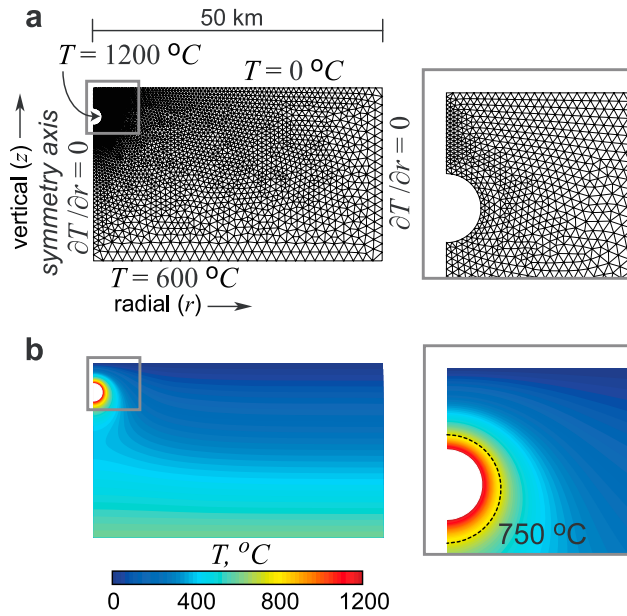


Figure 8. Thermal model. (a) Model configuration and FEM tessellation. Tomography data constrain the location and size of the magma reservoir (Figure 7), as well as the position of the Moho [Fliedner and Klemperer, 1999]. The base and top of the axisymmetric problem domain represent the Moho and the land surface, respectively. Vertical exaggeration is unity. (b) Temperature distribution. The 750°C isotherm marks the brittle-ductile transition. The three-dimensional problem domain is recovered by sweeping the two-dimensional slice, simulated by the FEM, about a vertical axis of symmetry centered on the caldera.

subscript k implies summation over these three components. In this formulation, x_1 , x_2 , and x_3 are equivalent to Cartesian coordinates x , y , and z (east, north, and vertical), respectively. Similarly, u_1 , u_2 , and u_3 are equivalent to u_x , u_y , and u_z , respectively. Viscoelastic behavior is simulated by imposing an additional stress-dependent creep relationship for the region representing the surrounding rind. The total uniaxial equivalent strain is

$$\varepsilon = \varepsilon_e + \varepsilon_f \quad \text{and} \quad \frac{d\varepsilon_f}{dt} = A\sigma_d^\eta, \quad (10)$$

where ε_e is the elastic strain, ε_f is the strain due to viscous flow, A is a constant that can be augmented to account for temperature dependence [Del Negro *et al.*, 2009], and σ_d is the deviatoric stress [Carter and Tsenn, 1987]. The relationship is equivalent to a Maxwell material for $\eta = 1$, and A is half of the inverse of the linear viscosity [Turcotte and Schubert, 2002]. Conceptually, the constant coeruption magma mass extraction will induce an accelerating depressurization of the magma reservoir over the duration of the eruption. The viscoelastic rind will deform via viscous flow to relax deviatoric stresses both during and after the eruption (following cessation of magma flux out of the reservoir). The total surface deformation is the combination of the elastic and viscous responses. The viscoelastic rind allows for two effects that are not available using purely elastic models, such as the one by Mogi [1958].

First, the flux out of the reservoir during the eruption induces transient posteruption deformation, even though flux is zero after the eruption. Second, as demonstrated later, the viscous contribution requires a lesser magnitude of depressurization to predict the observed deformation, in accord with lithostatic constraints, compared to a purely elastic counterpart.

[27] The axisymmetric problem is partitioned to allow for the distribution of rheologic and material properties according to the results of the thermal model (Figure 8) and local (Figure 7) and regional [Fliedner and Klemperer, 1999] seismic tomography. The problem domain configuration and specifications are given in Figure 9 and summarized in Table 2. The top of the problem domain, representing the land surface, is flat and a stress-free boundary. We neglect topographic effects [Cayol and Cornet, 1998], which are negligible for Okmok volcano because of its relatively low relief [Masterlark, 2007]. The far-field lateral boundary is merged with the basal boundary along an arc, along which displacements are zero, resulting in a hemispherical model domain.

[28] The lower portion of the problem domain (depth >30 km) represents the relatively stiff upper mantle. The upper portion and bulk of the problem domain represent the crust. The weak caldera partition is a quarter ellipse, abutting the axis of symmetry, with its major and minor half axes corresponding to the 5 km radius of the caldera and 2 km depth of the shallow LVZ, respectively. The specified elastic properties for the weak materials (Table 2) are chosen to simulate a ΔV_s contrast of about -10% , with respect to the crust, as constrained by the tomography data (Figure 7).

[29] The reservoir is simulated as a spherical cavity filled with a compressible fluid. We impose a mass flux to the cavity to simulate magma migration into or out of the reservoir. Changes in pressure within the reservoir (ΔP) and volume of the magma reservoir (ΔV) are solution variables. The reservoir is centered 5 km beneath the caldera and has a radius of 1500 m. The reservoir depth spans the expected range of neutral buoyancy for basaltic magma, and the base of the reservoir corresponds to the contractancy transition zone [Ryan, 1987b, 1994]. The viscoelastic rind surrounding the reservoir shares elastic properties with the basaltic crust, which are expected to be relatively constant over the predicted temperature range (Figure 8) [Ryan, 1987a]. The average viscosity of the rind, μ , and the coeruption mass flux, q_e , of the magma reservoir are calibration parameters. The problem domain is tessellated into 6791 first-order triangular finite elements. The characteristic length of the elements is about 100 m near the magma reservoir and increases to about 1000 m along the far-field boundary, where lower displacement gradients are expected. The 3-D problem domain for Okmok volcano is recovered by sweeping predictions about the vertical axis of symmetry (Figure 9c). We construct an auxiliary model to validate the elastic response of the FEM, in which a single set of elastic parameters are substituted into all problem domain partitions (Table 2). We use this FEM to calculate axisymmetric surface deformation and assume the far-field boundary is far enough away from the magma reservoir to approximate an elastic half-space. The FEM predictions are in agreement for the corresponding analytical solution [Mogi, 1958], which validates our configuration for the

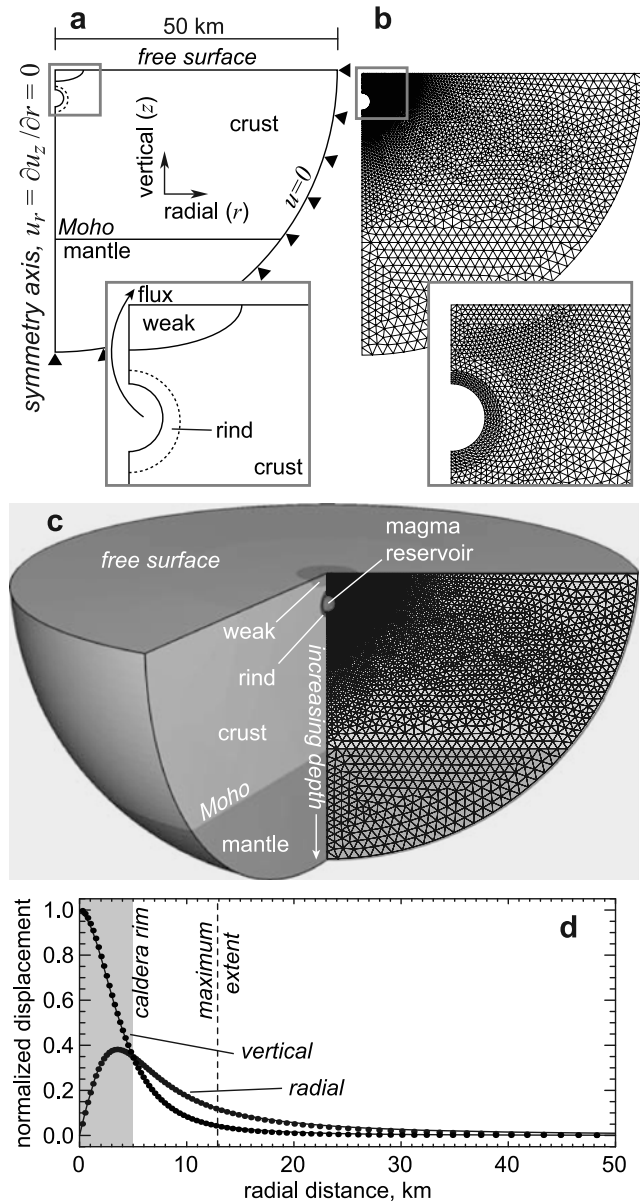


Figure 9. Deformation model. (a) FEM configuration. Vertical exaggeration is unity. (b) FEM tessellation. The 3-D problem domain is recovered by sweeping the 2-D slice, simulated by the FEM, about a vertical axis of symmetry centered on the caldera. Insets in both Figures 9a and 9b reveal the details of the simulated near-field region. (c) Three-dimensional problem domain. This cut-away representation (240° sweep) reveals the simulated 3-D structure of Okmok volcano. (d) FEM validation. Thin curves are predictions from analytical solutions [Mogi, 1958]. Black circles are FEM predictions. The shaded region delimits the caldera. The dashed line represents the maximum extent of the InSAR coverage from the center of the caldera.

FEMs to simulate deformation due to changes in pressure within a spherical cavity embedded in an elastic problem domain (Figure 9d).

[30] The 210 day separation of the initial eruption, 11 February 1997, and the acquisition date for the second

image used to construct the InSAR data (9 September 1997) is the total time interval of the transient simulations. Long-term deformation studies of Okmok suggest that flux into the magma reservoir decreased leading up to the two most recent eruptions in 1997 [Lu *et al.*, 2005; Mann *et al.*, 2002] and 2008 [Fournier *et al.*, 2009]. Deformation-based studies of other Aleutian volcanoes suggest eruption cycles are characterized by decaying rates of magma intrusion between eruptions [Lu *et al.*, 2003b]. Therefore, we ignore deformation during the 491 day interval separating the acquisition date (9 October 1995) of the first image used to construct the InSAR data and the eruption.

[31] The extraction of magma from the shallow reservoir drives the volcano deformation system. The extraction is simulated as a specified magma mass flux, $q(t)$, over the 210 day time step

$$q(t) = \begin{cases} q_e & \text{for } t_0 \leq t \leq t_1 \text{ (coeruption, 100 days)} \\ 0 & \text{for } t_1 < t \text{ (posteruption, 110 days)} \end{cases}, \quad (11)$$

where t_0 and t_1 represent the beginning and end of the 1997 eruption, respectively. Although we expect the magma mass flux out of the reservoir was not constant over the eruption interval, we cannot constrain variations of mass flux over the eruption interval with the temporal characteristics of the given InSAR data. For a similar model configuration of a pressurized magma reservoir embedded a viscoelastic material, Del Negro *et al.* [2009] demonstrated that the total deformation over a finite time interval is controlled by the net pressure load, rather than temporal variations of the load, over the finite time interval. This result validates our strategy for imposing a constant mass flux over the coeruption interval. The imposed mass flux couples to the predicted deformation for the surface of the volcano via (9) and (10) and specified density and bulk modulus parameters for the magma within the reservoir (Table 2). The time constant for the (Maxwell) viscoelastic relaxation is

$$\tau = \frac{2\mu}{E}, \quad (12)$$

where τ is the time constant, μ is viscosity, and E is Young's modulus [Turcotte and Schubert, 2002]. The characteristic viscosity for the 210 day time step spanning both coeruption and posteruption intervals is about 10^{18} Pa s.

[32] The InSAR data include deformation due to depressurization of the magma reservoir, combined with a plane shift to allow for uncertainties in the orbital positions [Massonnet and Feigl, 1998] and possibly strain accumulation due to plate convergence. The forward model for this system is

$$\mathbf{G}\mathbf{m} + \mathbf{d}_{\text{FEM}} = \mathbf{d}_{\text{pre}} \quad (13)$$

where \mathbf{G} is a matrix comprising column vectors of the x and y positions of each pixel and a unit column vector, \mathbf{m} is a column vector of three coefficients that account for the LOS plane shift, and \mathbf{d}_{FEM} is a vector of FEM displacement predictions for pixel locations resolved onto the LOS vector. The optimal $\mu - q$ combination minimizes the L_2 norm that was defined above [Aster *et al.*, 2005]. To achieve

this optimization, we predict surface deformation over a specified $\mu - q$ parameter space. Operationally, this optimization requires an automated system to configure and execute a unique FEM to predict deformation due to magma flux and estimate plane shift coefficients (13) for each of the a priori 6110 $\mu - q$ combinations. First, we construct a characteristic FEM having a configuration that is constant, except for $\mu - q$ specifications (Figures 9a and 9b). Second, we design and implement an algorithm that initializes the specified suite of parameter combinations comprising a discretized $\mu - q$ parameter space. For each $\mu - q$ combination, this algorithm then (1) duplicates the characteristic FEM, imposes $\mu - q$ specifications, and executes the FEM; (2) extracts surface deformation predictions, sweeps them about the axis of symmetry, interpolates the predictions to InSAR pixel locations, and projects the predicted displacement on the LOS vector; (3) estimates least squares estimates for the plane shift coefficients (\mathbf{m}) and calculates the LOS plane shift; and (4) calculates the L_2 norm.

[33] Computation times are strongly dependent on the particular $\mu - q$ pair of a given simulation. Solutions for FEMs having high μ and low q converge quickly. However, conjugate configurations of low μ and high q require several minutes to converge on a 64 bit PC capable of solving the entire problem in physical memory.

3. Results

[34] The shallow LVZ within the caldera extends to 2 km depth below the caldera floor (Figure 7d). This LVZ is probably the result of high fluid saturation and relatively low density of poorly consolidated material within the caldera. Eruptions at Okmok are known to display phreatomagmatic behavior and the bowl shape of the caldera funnels surface water and seasonal snowmelt toward the caldera center, forming several intracaldera lakes. The 2008 eruption of Okmok, centered north of Cone D, involved several nearby lakes in the eruption process. The shallow LVZ is an independent confirmation of previous studies that interpreted the caldera as being a mechanically weak zone [Mann *et al.*, 2002; Lu *et al.*, 2005] that acts as a lens through which deformation from greater depths is distorted [Masterlark, 2007]. Fluids within the caldera, associated with some combination of hydrothermal systems [Finney *et al.*, 2008], glacial melt, and groundwater [Larsen *et al.*, 2009], play a key role in this weakness of shallow caldera materials.

[35] The deep LVZ clearly indicates the presence of the magma reservoir beneath Okmok. The main part of this reservoir lies at depths greater than 4 km below the caldera floor and may be connected to the shallow LVZ by a thinner conduit-like structure. This depth is greater than GPS estimates, based on the simulations provided by Mogi [1958], from the same time period, which placed the chamber at 2.5 km below sea level (3 km below the caldera floor) [Fournier *et al.*, 2009]. It is interesting to note that the magma body at Okmok is a LVZ while, in a similar application of ANT, Brenguier *et al.* [2007] imaged an anomaly beneath Piton de la Fournaise as a high-velocity zone (HVZ). The difference may be explained by the interpretation of Brenguier *et al.* [2007] that the HVZ at

Piton de la Fournaise constituted a solidified magma intrusion. The fact the magma reservoir is imaged as an LVZ at Okmok points to it being in a molten state, at least in late 2005. This is further supported by the active deformation recorded on GPS instruments at Okmok during 2002–2005 [Fournier *et al.*, 2009], as well as InSAR data that suggest transient deformation during the interval 1992–2003 [Lu *et al.*, 2005]. It is likely that a significant portion of the reservoir remained molten during the entire intereruption period from 1997 until 2008. The bulk rheology implied by the tomography is essential to validating interpretations of volcano deformation. For example, several studies of Askja volcano, Iceland, suggest persistent, InSAR and GPS-observed transient deflation, in the absence of an eruption, is most likely due to magma migration downward from a shallow storage chamber [Pagli *et al.*, 2006]. This interpretation requires the molten state within the reservoir. A study of local tomography of Askja volcano could test this hypothesis.

[36] The misfit distribution over the flux-viscosity parameter space favors a flux range $(-4.5 < q_e < -4.0) \times 10^9$ kg/d and a viscosity less than 5×10^{17} Pa s (Figure 10). The InSAR data are best predicted by an FEM simulating the combination $q_e = -4.2 \times 10^9$ kg/d and $\mu = 7.5 \times 10^{16}$ (the preferred model). For $\mu \rightarrow \infty$, the viscous flow is null and the model approximates an elastic problem domain (10). Viscous flow is negligible over the 210 day combined coeruption and posteruption interval simulated by the FEMs for $\mu > 10^{19}$ ($\tau = 3000$ days) and $q_e = -4.4 \times 10^9$ kg/d represents the best fully elastic FEM. The maximum magnitude of the transient pressure change is in accord with lithostatic conditions and decays after the eruption ends (Figures 10b and 10c). Deformation predictions and residuals are shown in Figure 11 and summarized in Table 3 for the three competing models: Homogeneous elastic half-space, FEM elastic, and (preferred) FEM viscoelastic.

[37] The FEM having the optimal $\mu - q$ combination satisfies our objectives of predicting the InSAR data with a deformation model that simulates mass extraction from the magma reservoir, while simultaneously accounting for the material property configuration of the tomography and reducing the magnitude of depressurization to within lithostatic constraints. The presence of the viscoelastic rind is the key to this result. Integration of the estimated flux $(-4.2 \times 10^9$ kg/d) over the 100 day interval of the 1997 eruption is scaled by the inverse of the magma density (~ 3000 kg/m³) and converted to an equivalent volume of -0.14 km³. This volumetric extraction of magma is remarkably consistent with the dense rock volume of the lava flows extruded during of the 1997 eruption, which is estimated to range from 0.07 to 0.14 km³ [Lu *et al.*, 2003a].

4. Discussion

[38] We interpret the coeruption InSAR data as a manifestation of an impulse-response mechanism (Figure 12) and envision the following sequence of events leading up to, during, and shortly after the 1997 eruption of Okmok volcano. A magma supply from a deep source replenishes the shallow magma reservoir (deep LVZ), until the pressure in this reservoir becomes critical by exceeding the sum of the lithostatic pressure and the tensile strength of the rock

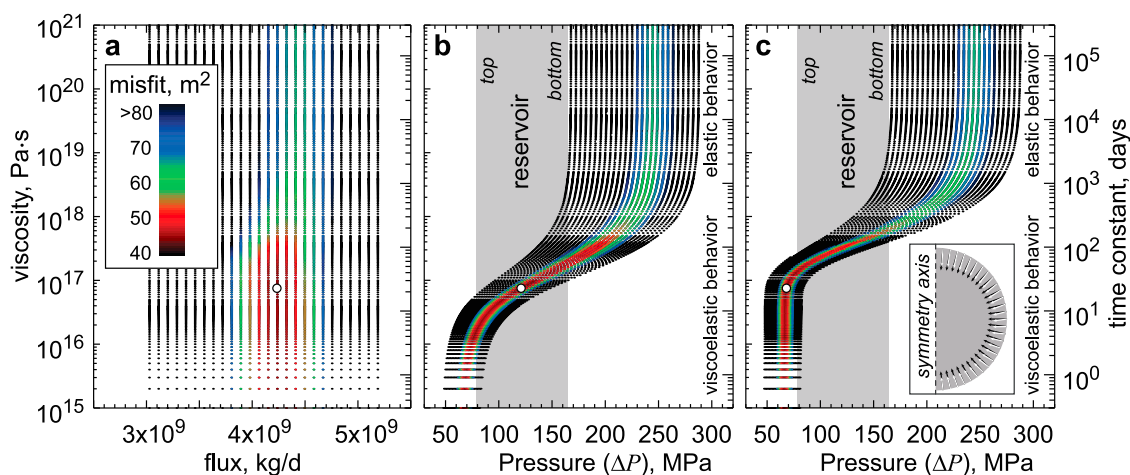


Figure 10. Misfit for flux-viscosity-pressure parameter space. Each dot represents misfit from an FEM having the corresponding pair of parameters. Flux and pressure are expressed as magnitudes. White circles represent the minimum misfit model. Vertical scales are viscosity and corresponding time constant (12) on the left and right side of each plot, respectively. (a) Flux-viscosity misfit. The misfit color legend applies to all plots in this composite. (b) Pressure-viscosity: end of 1997 eruption. Gray region represents the lithostatic pressure ranging from the top to the bottom of the magma reservoir. For the minimum misfit model, the specified mass flux induces a pressure change similar to the lithostatic pressure at the depth calculated for the center of the magma reservoir. (c) Pressure-viscosity: posteruption. For the minimum misfit model, the change in pressure within the magma relaxes and is less than the calculated lithostatic pressure of the magma reservoir. The misfit of the best fit viscoelastic model is about half that of the best fit elastic model. Predictions for models having viscosities greater than 10^{19} Pa s are indistinguishable from those of an elastic model for the time intervals considered. Inset shows reservoir deformation. Gray hemisphere is the initial shape of the axisymmetric reservoir. Best fit viscoelastic (black vectors) and elastic models (white vectors) represent total displacement over the 210 day time step ($100 \times$ exaggeration). Displacements nearing the off-axis margin move downward for the elastic model, compared to the viscoelastic model, resulting in different deformed source shapes for the different rheologic configurations.

[Wang, 2000]. We take a processes-oriented perspective and define a “dike” as a magma-filled crack [e.g., Buck *et al.*, 2006; Rubin, 1995]. A dike initiates from the wall of the reservoir, propagates to the land surface, and the eruption ensues. Magma is transported from the magma reservoir at a constant mass flux and extruded on the caldera floor over the interval of the eruption. During this time, the magma reservoir depressurization is modulated by viscoelastic relaxation of the surrounding rind, which accelerates the volumetric strain of the magma reservoir. Cessation of mass flux marks the end of the eruption. Following the eruption (and cessation of coeruption mass flux), viscous flow continues to relax deviatoric stresses within the viscoelastic rind. The decaying rate of repressurization within the reservoir following the eruption emulates a hydraulic model for magma movement, for which the flow rate is proportional to the pressure gradient between the reservoir and a source at depth having constant pressure [Dvorak and Okamura, 1987; Lu *et al.*, 2003b; Turcotte and Schubert, 2002]. This ongoing coupling of pressure within the magma reservoir and viscoelastic relaxation of the surrounding rind induces continued deformation of the land surface.

[39] Interpretations of deformation for Okmok volcano based on this proposed impulse-response behavior and a problem domain having a distribution of material properties are markedly different from interpretations based on con-

ventional homogeneous elastic half-space models [e.g., Mogi, 1958] for Okmok volcano in two ways. First, the impulse-response behavior proposed here allows for transient processes other than the static response due to incremental addition or removal of magma from the reservoir. This transience allows for smaller impulse magnitudes to generate a given magnitude of deformation, compared to static response models (Figure 10). For static response models, interpretations of deformation are attributed to linear coeval magma intrusion, i.e., volcano inflation observed with InSAR for a given time span indicates magma intrusion over the corresponding time span. In contrast, interpretations of deformation using impulse-response models proposed here may involve the continued deformation long after cessation of magma intrusion. Thus, deformation-based inferences of time-dependent magma supply dynamics strongly depend on the rheology of the model used to interpret the deformation data. Second, the images constructed from surface wave group velocity and shear wave tomography and depth inversion (Figure 7), contain two striking LVZs. These tomography data require a heterogeneous distribution of material properties, having both lateral and vertical variations, for Okmok volcano. Deviations from the homogeneous material property assumption of Mogi [1958] are known to significantly impact deformation predictions, particularly for lateral variations in material prop-

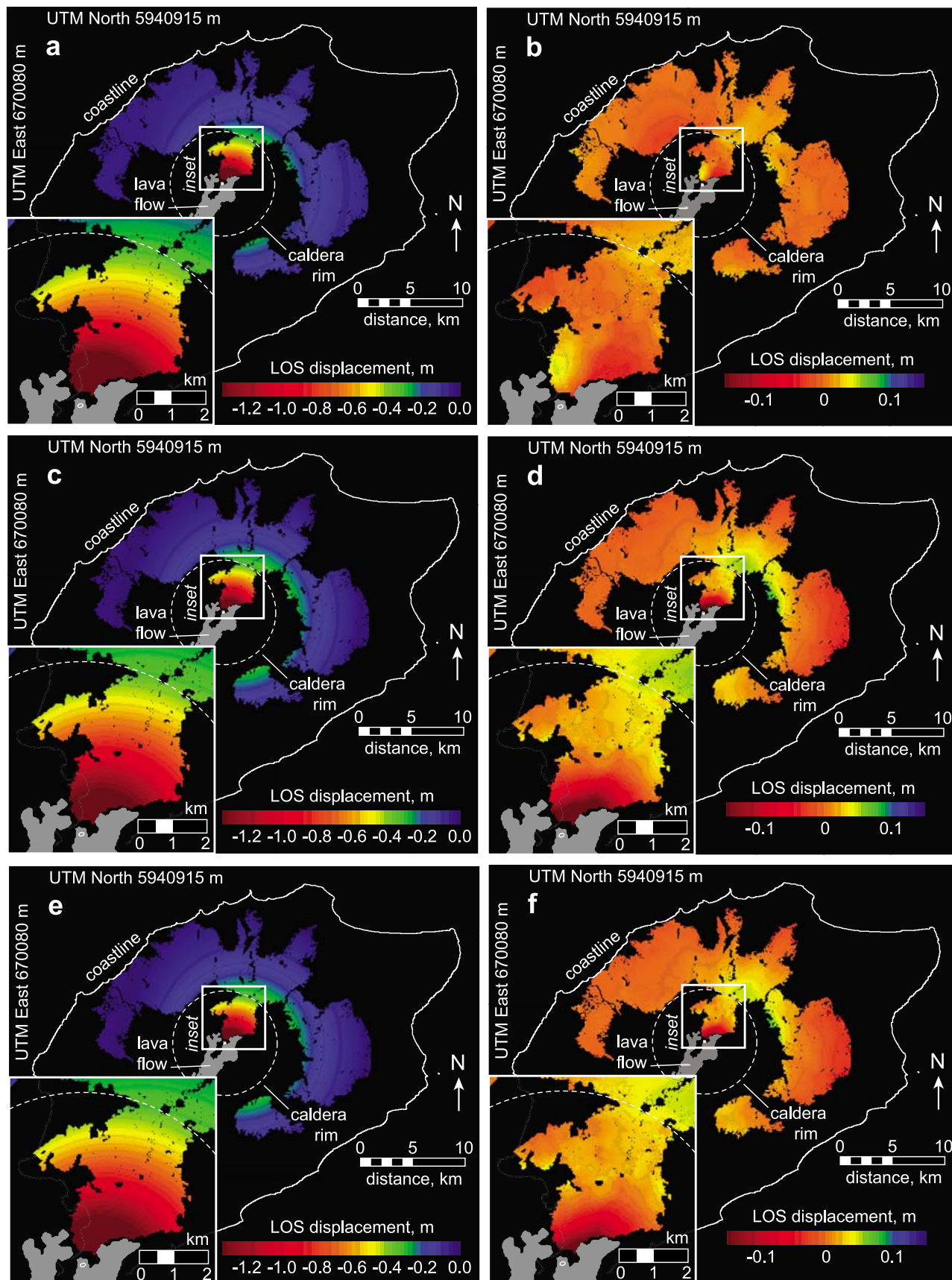


Figure 11

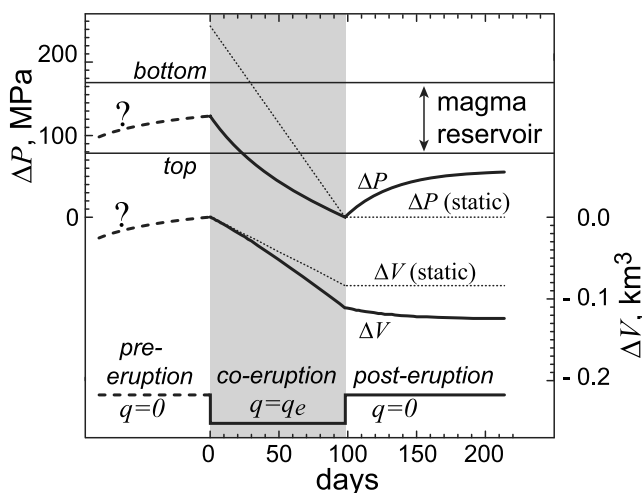


Figure 12. Magma flux and reservoir deformation. The model is driven by a constant flux of -4.2×10^9 kg/d during the eruption interval. The thick black top and middle curves represent the transient ΔP and ΔV , respectively, for the magma reservoir embedded in a viscoelastic rind ($\mu = 7.5 \times 10^{16}$ Pa s). The thick curve near the bottom represents the imposed flux, $q(t)$. Solid portions of these curves correspond to the 210 day simulation, which comprises the 100 day coeruption interval and 110 day posteruption interval that terminates with the acquisition of the second SAR image. Notice the transient effects continue after cessation of the coeruption magma flux. Thin dotted curves simulate the same flux for a model that does not include viscoelastic effects (static). Thin solid horizontal lines span the range of lithostatic pressure over the magma reservoir.

erties [Bianchi et al., 1987; De Natale and Pingue, 1996; Masterlark, 2007; Trasatti et al., 2007].

[40] The model by Mogi [1958] overpredicts deformation in the region immediately to the east of the western and smaller lobe of the 1997 lava flow (Figure 11b). The residual spatial patterns of the best elastic and viscoelastic FEMs are very similar to one another, but differ from the models by Mogi [1958], and indicate the FEMs systematically underpredict deformation near the center of the caldera, to the north of the eastern lobe of the 1997 lava flow (Figures 11d and 11f). This disparity arises from two differences between the configuration of Mogi [1958] versus that of the FEMs, which result in relatively suppressed deformation gradients for FEM-predicted deformation near the center of the caldera. First, the model by Mogi [1958] approximates a point source, which does not account for the finite size of the magma reservoir [McTigue, 1987]. This effect produces a more peaked deformation pattern [Masterlark, 2007]. Second, the shallow weak materials of the FEMs flatten the deformation pattern within the caldera region [Masterlark, 2007].

[41] Interestingly, the configuration given by Mogi [1958] produced the least misfit (13.8 m^2) of the InSAR data among the models tested in this analysis (Table 3). The best misfits of the elastic and viscoelastic FEMs are 64.0 and 44.7 m^2 , respectively (Table 3). On one hand, we could interpret this result by stating that the simplest model [Mogi, 1958] fits the InSAR data best and thereby rejecting the more complicated FEMs. However, the price of neglecting the tomography data is that the inferred characteristics of the magma reservoir using a model given by Mogi [1958] are severely biased by the invalid assumption of a homogeneous problem domain. In this case, the magnitude of required pressurization is an order of magnitude greater than lithostatic conditions for the optimized depth of the magma reservoir. Furthermore, ignoring the weak caldera material leads to a significant underestimation of the magma reservoir depth [Masterlark, 2007]. These unrealistic results, combined with the imaged heterogeneous structure of the shallow LVZ, are clear indicators that a homogeneous elastic half-space model is a poor approximation of the natural deformational system of Okmok volcano. Previous estimates of source characteristics for deformation of Okmok volcano are clearly at odds with those of this study. We propose that this discrepancy is a manifestation of precision versus accuracy. On the basis of the ideal shape of the observed coeruption and posteruption deformation patterns for Okmok volcano, models given by Mogi [1958] can, indeed, estimate precise deformation source parameters [Fournier et al., 2009; Lu et al., 2005; Masterlark, 2007] (Figure 2). However, the resulting estimations are probably not accurate, because they do not account for the rheologic structure of the volcano revealed by the new seismic tomography and thermal model predictions presented in this study.

[42] On the basis of the tomography data (Figure 7) and FEMs, we propose that the underprediction is the combined result of the emplacement of the lava flows and post-emplacment processes, which are not accounted for in the deformation models. Previous studies of several volcanoes link InSAR-based deformation of erupted materials to a variety of processes, such as compaction, thermoelastic contraction, poroelastic effects, and viscoelastic relaxation [Briole et al., 1997; Lu et al., 2005; Masterlark et al., 2006; Stevens et al., 2001]. Results suggest that deformation of the erupted materials, as well as the surrounding substrate can be several centimeters. For the case of the InSAR data and model predictions presented here for the 1997 eruption of Okmok volcano, we suggest that the total deformation pattern is the net result of a mass flux extraction from the magma reservoir, posteruption viscoelastic deformation of the rind surrounding the magma chamber, and local posteruption subsidence due to the emplacement of the lava flows that are several tens of meters thick [Lu et al., 2000, 2005]. The local subsidence due to the emplaced lava flow, combined with the volcano-wide subsidence due to magmatic flux,

Figure 11. Deformation predictions and residual. Positive LOS displacement of the land surface is toward the satellite. Small white ellipse at center of caldera is the estimated horizontal location of the magma reservoir and axis of vertical symmetry (Figure 2). (a) Homogeneous elastic half-space [Mogi, 1958], predicted. (b) Homogeneous elastic half-space, residual. (c) FEM elastic, predicted. (d) FEM elastic, residual. (e) FEM viscoelastic, predicted. (f) FEM viscoelastic, residual. The pattern of the residual is sensitive to the material property distribution required by the tomography.

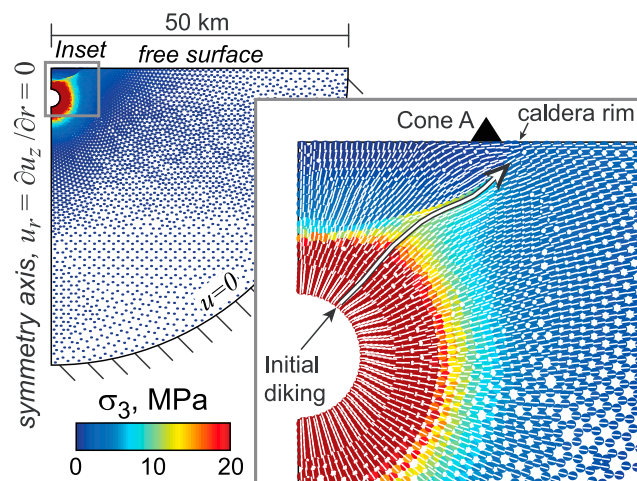


Figure 13. Coeruption stress. Colored dots represent the predicted minimum principal stresses (σ_3) calculated for the centroidal position of each element. Extension is positive. The inset shows details of the stress distribution near the caldera. White line segments represent maximum principal stress (σ_1) trajectories within the plane of radial symmetry. The stress distribution and orientation favor a dike initiating from the reservoir and propagating both upward and outward along σ_1 trajectories.

gives a net subsidence pattern that is peaked near the center of the caldera. This explains the apparently better misfit characteristics of the model given by Mogi [1958], compared to the FEMs (Table 3). The quantitative predictions of deformation associated with lava emplacement may substantially improve the misfit of the FEMs. The geometric shape of the deformation source is an additional complexity that will also influence the shape of the deformation pattern. A relatively simple case is presented by the deformed shape of the initially spherical magma reservoir, which will differ because of elastic versus viscoelastic rheologic configurations simulated in this study (Figure 10c, inset). These differences account for the variations in depth of the misfit “trough” that tracks the viscosity parameter space. More significant departures from a spherical source geometry [e.g., Masterlark and Lu, 2004, and references therein] can substantially change deformation predictions.

[43] The FEM predicts that the maximum hoop stress is about midway up the upper hemisphere of the effective reservoir and corresponds to the point of tangency along a line extending from the axis of symmetry at the free surface and tangent to the magma reservoir [McTigue, 1987]. The maximum principle stress trajectories favor propagation of a dike outward from this point [Gudmundsson, 2002] (Figure 13). The coeruption stress regime predicted by the FEM, with its heterogeneous material property partitioning, is consistent with vertical dike arrest due to the material property contrast along the base of the shallow LVZ [Gudmundsson, 2002; Gudmundsson and Loetveit, 2005; Gudmundsson and Philipp, 2006]. In this case, magma propagation continues upward and outward from the reservoir and follows maximum principle stress trajectories [Rubin, 1995] along the base of the shallow LVZ. The shallow LVZ is presumably a region of low density. The

density contrast at the base of the shallow LVZ would then be a likely horizon of neutral buoyancy, providing a strong guide for lateral magma migration from the center of the caldera outward toward the rim of the caldera [Ryan, 1987a, 1987b, 1994]. Both the predicted coeruption stress regime and expected horizon of neutral buoyancy associated with the presence of the shallow LVZ account for the lava extrusion of the 1997 eruption from Cone A, near the caldera rim.

[44] Okmok volcano has since erupted in July 2008. Forthcoming studies will present InSAR data for this latest eruption. Thus, we will have InSAR data covering the complete 1997/2008 eruption cycle. Previous studies attempted to characterize the plumbing system of Okmok volcano, based on InSAR-observed deformation before, during, and after the 1997 eruption [Lu et al., 2005]. More recently, Fournier et al. [2009] investigated the post-1997 eruption behavior of the shallow source using continuous GPS. The sequence of historic eruptions for Okmok volcano suggests an eruption every 10–20 years (Figure 1a). Mann et al. [2002] used geodetic data associated with the 1997 eruption and proposed a plumbing system for Okmok volcano, but wisely pointed out that the plumbing system itself is transient based on the multiple cones along the rim of the caldera. This transience is manifest in the 2008 eruption emanating from new craters near Cone D [Larsen et al., 2009], rather than Cone A of the 1997 eruption (Figure 1b). Newly emplaced lava flows alter the stress regime of the shallow caldera and thus influence the path of magma from the reservoir to the land surface during subsequent eruptions. These systematic loading events may account for the changes in eruption locations within the caldera.

[45] Previous studies of deformation for Okmok volcano are subject to static requirements of linear elastic deformation models [Mogi, 1958; Okada, 1992], where an increment of deformation corresponds to an increment of magma flux at depth. In this case, time sequences of InSAR or GPS data are simulated in terms of corresponding time sequences of magma flux and generally interpreted as a continuous, but variable, magmatic flux from a deeper source [Lu et al., 2005; Mann et al., 2002]. An implication of this continuous flux is that there is a conduit connecting the deep magma source and shallow reservoir, and it is always open. Discrete magma pulses from some source at depth provide an alternative mechanism for magma replenishment. A necessary requirement for elastic models of these finite pulses is that the dike walls close behind the rising magma, although some magma must remain behind because of viscous resistance [Rubin, 1995]. Assuming a magma velocity of a few millimeters per second, based on posteruption pulses inferred from geodetic data [Fournier et al., 2009], this residual magma would likely freeze, unless the residual thickness was more than several meters [Turcotte and Schubert, 2002].

[46] We extend the magma pulse mechanism implied in this analysis and present an alternative hypothesis for time-dependent deformation of Okmok volcano. The single impulse-response mechanism of the coeruption InSAR data is expanded to the convolution of a series of discrete magma flux pulses and viscoelastic relaxation episodes. If we

assume that the 1997 and 2008 eruptions span a complete eruption cycle for Okmok volcano, we can envision that the pressure gradient between the shallow magma reservoir and a deeper source is maximized after the 1997 eruption. A series of magma pulses recharge the shallow reservoir. The magnitude of each successive pulse is decreased with the decreasing pressure gradient between the shallow reservoir and deeper magma source. Ultimately, the cumulative pressure in the shallow reservoir from these magma pulses reaches a critical state, a dike propagates upward, and the 2008 eruption ensued. For this proposed impulse-response sequence, there is no need for an open conduit connecting the shallow magma chamber and the deeper magma source.

[47] The choice of either a traditional open conduit model or our proposed impulse-response model will strongly influence interpretations of transient deformation of Okmok volcano in terms of magma replenishment. *Fournier et al.* [2009] identify several distinct pulses of inflation during the 1997 posteruption interval. For an open conduit model, the predicted volume change is integrated over time to estimate the net volume of magma replenishment [*Fournier et al.*, 2009; *Lu et al.*, 2005; *Miyagi et al.*, 2004]. Alternatively, a finite pulse of magma intrusion, followed by viscoelastic relaxation gives a different picture of magma replenishment. Simulations of the deformation due to lava loads, comprehensive exploration of parameter space associated with more complicated source geometry configurations, and evaluation of the proposed impulse-response model for InSAR, GPS, and seismicity data that span the 1997–2008 eruption cycle are subjects of ongoing research.

5. Conclusions

[48] InSAR data reveal that the caldera of Okmok volcano, Alaska, subsided more than a meter during its eruption in 1997. Because of the strong radial symmetry and high signal-to-noise ratio of the InSAR data, inverse analyses of InSAR data precisely define the source of deformation as an effectively spherical pressure source region (-5.5×10^8 Pa) at a depth of 3.1 km. These characteristics severely exceed lithostatic pressure constraints. Seismic tomography images reveal a significantly deeper magma reservoir (>4 km) and a low-velocity zone corresponding to a layer of weak materials within the caldera, extending from the caldera surface to a depth of 2 km. The InSAR data are well predicted by an FEM that accounts for the tomography and simulates a mass flux of -4.2×10^9 kg/d from the magma reservoir during the eruption interval and includes a rind viscosity of 7.5×10^{16} Pa s. The integrated magma flux agrees with the observed quantity of magma extrusion. The shallow weak layer within the caldera provides a coeruption stress regime and neutral buoyancy horizon that support lateral magma propagation from the central magma reservoir to extrusion near the rim of the caldera. Both of these effects explain the lateral offset of the magma extrusion compared to the location of the magma chamber beneath the center of the caldera. FEMs that include these geometric constraints and variations in material properties allow us to reduce the estimated depressurization of the magma reservoir, while simultaneously maintaining the magnitude of deformation required to predict the InSAR data. Interpretations of magmatic migration and storage, based on deformation models

that simulate the observed rheological structure and are calibrated to deformation data, are markedly different from interpretations estimated from homogeneous elastic half-space models calibrated to deformation data alone. Knowledge and integration of the subsurface structure and rheology are prerequisite for reliable quantitative analyses of volcano deformation.

Notation

A	flow coefficient, $(\text{Pa s})^{-1}$.
\mathbf{B}	elastic property-dependent matrix.
c	phase velocity, s^{-1} .
\mathbf{d}_{FEM}	FEM prediction vector.
\mathbf{d}_{obs}	observed data vector.
\mathbf{d}_{pre}	net prediction vector.
d	time sample, dimensionless.
E	Young's modulus, Pa.
F	body force per unit volume, N m^{-3} .
G	shear modulus, Pa.
\mathbf{G}	plane shift matrix.
i	coordinate indices, dimensionless.
j	data vector indices, dimensionless.
k	implied summation of coordinate indices.
\mathbf{K}_c	phase velocity kernel matrix.
\mathbf{K}_g	group velocity kernel matrix.
K	bulk modulus, Pa.
L_2	residual sum of squares, m^2 .
\mathbf{M}	density-dependent matrix.
M	number of tomography elements, dimensionless.
\mathbf{m}	plane shift vector.
m	summation index, dimensionless.
N	window half-length, dimensionless.
n	time sample index, dimensionless.
ΔP	pressure change within magma reservoir, Pa.
q	magma flux into reservoir, kg s^{-1} .
q_e	coeruption magma flux into reservoir, kg s^{-1} .
R	Euclidean distance, m.
r_s	radius of sphere, m.
\mathbf{S}_{xy}	correlation matrix, position couples for axis of symmetry.
\mathbf{S}_{Pd}	correlation matrix, source depth and pressure couples.
s	spherical expansion source strength, m^3 .
t	time, s.
T	temperature, $^{\circ}\text{C}$.
u	displacement, m.
u^*	unit impulse response function, m^{-2} .
V	volume of magma reservoir, m^3 .
ΔV	change in volume of magma reservoir, m^3 .
V_g	group velocity, m s^{-1} .
V_p	P wave velocity, m s^{-1} .
V_s	S wave velocity, m s^{-1} .
\mathbf{v}	eigenvector.
w	Rayleigh wave number, dimensionless.
W	time sample weighting factor, dimensionless.
x	Cartesian coordinate corresponding to east, m.
x_0	location of symmetry axis (east), m.
y	Cartesian coordinate corresponding to north, m.
y_0	location of symmetry axis (north), m.
z	Cartesian coordinate corresponding to vertical, m.
ε	strain, dimensionless.

- ϵ_e elastic strain, dimensionless
 ϵ_f viscous strain, dimensionless.
 η power law exponent, dimensionless.
 μ Maxwell viscosity, Pa s.
 ν Poisson's ratio, dimensionless.
 ξ position of deformation source, m.
 ρ density, kg m⁻³.
 σ stress, Pa.
 σ_d deviatoric stress, Pa.
 σ_1 maximum principal stress, Pa.
 σ_3 minimum principal stress, Pa.
 τ viscoelastic time constant, s.
 ω frequency, Hz.

[49] **Acknowledgments.** This work is supported in part by U.S. Geological Survey/ARRA award G10AC00039 and the U.S. Geological Survey Mendenhall Program. Academic licensing for Abaqus software is provided by Simulia, Dassault Systèmes. Insightful reviews by Michael P. Ryan (Associate Editor), Andrew Newman, and an anonymous reviewer greatly improved this paper. Matthew Haney wishes to thank David Aldridge for access to the 2-D tomography code PRONTO. Timothy Masterlark thanks Kurt Feigl, Allan Rubin, and Clifford Thurber for helpful discussions and guidance. James Dixon kindly provided assistance with the seismicity catalog of the Alaska Volcano Observatory, U.S. Geological Survey.

References

- Aki, K. (1957), Space and time spectra of stationary stochastic waves, with special reference to microtremors, *Bull. Earthquake Res. Inst. Univ. Tokyo*, 25, 415–457.
- Aki, K. (1965), A note on the use of microseisms in determining the shallow structures of the Earth's crust, *Geophysics*, 30, 665–666, doi:10.1190/1.1439640.
- Aki, K., and P. Richards (1980), *Quantitative Seismology*, vol. 1, 557 pp., W. H. Freeman, New York.
- Aldridge, D. F., and D. W. Oldenburg (1993), Two-dimensional tomographic inversion with finite-difference traveltimes, *J. Seismic Explor.*, 2, 257–274.
- Aster, R., B. Borchers, and C. Thurber (2005), *Parameter Estimation and Inverse Problems*, 301 pp., Elsevier, Dordrecht, Netherlands.
- Begét, J. E., J. F. Larsen, C. A. Neal, C. J. Nye, and J. R. Schaefer (2005), Preliminary volcano-hazard assessment for Okmok volcano, Umnak island Alaska, *DGGs Rep. Invest.*, 2004-3, 32 pp., Alaska Dep. of Nat. Resour., Fairbanks.
- Bensen, G. D., M. H. Ritzwoller, M. P. Barmin, A. L. Levshin, F. Lin, M. P. Moschetti, N. M. Shapiro, and Y. Yang (2007), Processing seismic ambient noise data to obtain reliable broad-band surface wave dispersion measurements, *Geophys. J. Int.*, 169, 1239–1260, doi:10.1111/j.1365-246X.2007.03374.x.
- Bianchi, R., A. Coradini, C. Federico, G. Gilberti, P. Lanciano, J. P. Pozzi, F. Sartoris, and R. Scandone (1987), Modelling of surface ground deformation in volcanic areas: The 1970–1972 and 1982–1984 crises of Campi Flegrei, Italy, *J. Geophys. Res.*, 92, 14,139–14,150, doi:10.1029/JB092iB13p14139.
- Brenguier, F., N. M. Shapiro, M. Campillo, A. Nercessian, and V. Ferrazzini (2007), 3-D surface wave tomography of the Piton de la Fournaise volcano using seismic noise correlations, *Geophys. Res. Lett.*, 34, L02305, doi:10.1029/2006GL028586.
- Brenguier, F., N. M. Shapiro, M. Campillo, V. Ferrazzini, Z. Duputel, O. Coutant, and A. Nercessian (2008a), Toward forecasting eruptions using seismic noise, *Nat. Geosci.*, 1, 126–130, doi:10.1038/ngeo104.
- Brenguier, F., M. Campillo, C. Hadziioannou, N. M. Shapiro, R. M. Nadeau, and E. Larose (2008b), Postseismic relaxation along the San Andreas fault at Parkfield from continuous seismological observations, *Science*, 321, 1478–1481, doi:10.1126/science.1160943.
- Briole, P., D. Massonnet, and C. Delacourt (1997), Post-eruptive deformation associated with the 1986–87 and 1989 lava flows of Etna detected by radar interferometry, *Geophys. Res. Lett.*, 24, 37–40, doi:10.1029/96GL03705.
- Buck, W. R., P. Einarsson, and B. Brandsdóttir (2006), Tectonic stress and magma chamber size as controls on dike propagation: Constraints from the 1975–1984 Krafla rifting episode, *J. Geophys. Res.*, 111, B12404, doi:10.1029/2005JB003879.
- Burgisser, A. (2005), Physical volcanology of the 2050 BP caldera-forming eruption of Okmok volcano, Alaska, *Bull. Volcanol.*, 67, 497–525, doi:10.1007/s00445-004-0391-5.
- Byers, F. M., Jr., D. M. Hopkins, K. L. Wier, and B. Fisher (1947), Volcano investigations on Umnak Island, 1946, part III, *U.S. Geol. Surv. Alaskan Volcano Invest. Rep.*, 2, pp. 19–53, U.S. Geol. Surv., Reston, Va.
- Caplan-Auerbach, J., S. C. Moran, G. Tytgat, T. A. Plucinski, S. R. McNutt, and J. R. Paskievitch (2004), Seismic explorations in the eastern Aleutians, Alaska, *Seismol. Res. Lett.*, 75, 8–21, doi:10.1785/gssrl.75.1.8.
- Carter, N. L., and M. C. Tsenn (1987), Flow properties of continental lithosphere, *Tectonophysics*, 136, 27–63, doi:10.1016/0040-1951(87)90333-7.
- Cayol, V., and F. H. Cornet (1998), Effects of topography on the interpretation of the deformation field of prominent volcanoes—Application to Etna, *Geophys. Res. Lett.*, 25, 1979–1982, doi:10.1029/98GL51512.
- Christensen, N. I. (1996), Poisson's ratio and crustal seismology, *J. Geophys. Res.*, 101, 3139–3156, doi:10.1029/95JB03446.
- Claerbout, J. F. (1968), Synthesis of a layered medium from its acoustic transmission response, *Geophysics*, 33, 264–269, doi:10.1190/1.1439927.
- Cross, R. S., and J. T. Freymueller (2008), Evidence for and implications of a Bering plate based on geodetic measurements from the Aleutians and western Alaska, *J. Geophys. Res.*, 113, B07405, doi:10.1029/2007JB005136.
- Davis, J. C. (2002), *Statistics and Data Analysis in Geology*, 639 pp., John Wiley, New York.
- Dehn, J., K. Dean, and K. Engle (2000), Thermal monitoring of North Pacific volcanoes from space, *Geology*, 28, 755–758, doi:10.1130/0091-7613(2000)28<755:TMONPV>2.0.CO;2.
- Del Negro, C., G. Currenti, and D. Scandura (2009), Temperature-dependent viscoelastic modeling of ground deformation: Application to Etna volcano during the 1993–1997 inflation period, *Phys. Earth Planet. Inter.*, 172, 299–309, doi:10.1016/j.pepi.2008.10.019.
- De Natale, G., and F. Pingue (1996), Ground deformation modeling of volcanic areas, in *Monitoring and Mitigation of Volcanic Hazards*, edited by R. Scarpa and R. I. Tilling, pp. 365–388, Springer, Berlin.
- Dixon, J. P., S. D. Stihler, J. A. Power, G. Tytgat, S. C. Moran, J. Sanchez, S. Estes, S. R. McNutt, and J. Paskievitch (2003), Catalog of earthquake hypocenters at Alaskan volcanoes: January 1 through December 31, 2002, *U.S. Geol. Surv. Open File Rep.*, OF 03-0267, 58 pp.
- Dixon, J. P., S. D. Stihler, J. A. Power, G. Tytgat, S. C. Moran, J. J. Sanchez, S. R. McNutt, S. Estes, and J. Paskievitch (2004), Catalog of earthquake hypocenters at Alaskan volcanoes: January 1 through December 31, 2003, *U.S. Geol. Surv. Open File Rep.*, OF 2004-1234, 69 pp.
- Dixon, J. P., S. D. Stihler, J. A. Power, G. Tytgat, S. Estes, S. Prejean, J. J. Sanchez, R. Sanches, S. R. McNutt, and J. Paskievitch (2005), Catalog of earthquake hypocenters at Alaskan volcanoes: January 1 through December 31, 2004, *U.S. Geol. Surv. Open File Rep.*, 2005-1312, 74 pp.
- Dixon, J. P., S. D. Stihler, J. A. Power, G. Tytgat, S. Estes, and S. R. McNutt (2006), Catalog of earthquake hypocenters at Alaskan volcanoes: January 1 through December 31, 2005, *U.S. Geol. Surv. Open File Rep.*, 2006-1264, 78 pp.
- Dixon, J. P., S. D. Stihler, and J. D. Power (2008a), Catalog of earthquake hypocenters at Alaskan volcanoes: January 1 through December 31, 2007, *U.S. Geol. Surv. Data Ser.*, 367, 82 pp., U.S. Geol. Surv., Reston, Va.
- Dixon, J. P., S. D. Stihler, J. A. Power, and C. Searcy (2008b), Catalog of earthquake hypocenters at Alaskan volcanoes: January 1 through December 31, 2006, *U.S. Geol. Surv. Data Ser.*, 326, 79 pp., U.S. Geol. Surv., Reston, Va.
- Dobran, F. (2001), *Volcanic Processes: Mechanisms in Material Transport*, 590 pp., Kluwer, New York.
- Dragoni, M., and C. Magnanensi (1989), Displacement and stress produced by a pressurized, spherical magma chamber, surrounded by a viscoelastic shell, *Phys. Earth Planet. Inter.*, 56, 316–328, doi:10.1016/0031-9201(89)90166-0.
- Dvorak, J., and A. T. Okamura (1987), A hydraulic model to explain variations in summit tilt rate at Kilauea and Mauna Loa volcanoes, in *Volcanism in Hawaii*, vol. 2, edited by R. W. Decker, T. L. Wright, and P. H. Stauffer, *U.S. Geol. Surv. Prof. Pap.*, 1350, 1281–1296.
- Finney, B., S. Turner, C. Hawkesworth, J. Larsen, C. Nye, R. Grorge, I. Bindeman, and J. Eichelberger (2008), Magmatic differentiation at an island-arc caldera: Okmok volcano, Aleutian islands, Alaska, *J. Petrol.*, 49, 857–884, doi:10.1093/petrology/egn008.
- Fliedner, M. M., and S. L. Klemperer (1999), Structure of an island-arc: Wide angle seismic studies in the eastern Aleutian Islands, Alaska, *J. Geophys. Res.*, 104, 10,667–10,694, doi:10.1029/98JB01499.
- Fournier, T., J. Freymueller, and P. Cervelli (2009), Tracking magma volume recovery at Okmok volcano using GPS and an unscented Kalman filter, *J. Geophys. Res.*, 114, B02405, doi:10.1029/2008JB005837.
- Gerstoft, P., K. G. Sabra, P. Roux, W. A. Kuperman, and M. C. Fehler (2006), Green's function extraction and surface-wave tomography from microseisms in southern California, *Geophysics*, 71, S123–S131, doi:10.1190/1.2210607.

- Gudmundsson, A. (2002), Emplacement and arrest of sheets and dykes in central volcanoes, *J. Volcanol. Geotherm. Res.*, *116*, 279–298, doi:10.1016/S0377-0273(02)00226-3.
- Gudmundsson, A., and I. F. Loetveit (2005), Dyke emplacement in a layered and faulted rift zone, *J. Volcanol. Geotherm. Res.*, *144*, 311–327, doi:10.1016/j.jvolgeores.2004.11.027.
- Gudmundsson, A., and S. Philipp (2006), How local stress fields prevent volcanic eruptions, *J. Volcanol. Geotherm. Res.*, *158*, 257–268, doi:10.1016/j.jvolgeores.2006.06.005.
- Hirth, G., J. Escartin, and J. Lin (1998), Rheology of the lower oceanic crust: Implications for lithospheric deformation at mid-ocean ridges, in *Faulting and Magmatism at Mid-Ocean Ridges*, *Geophys. Monogr. Ser.*, vol. 106, edited by W. R. Buck et al., pp. 291–303, AGU, Washington, D. C.
- House, L. S., and K. H. Jacob (1983), Earthquakes, plate subduction, and stress reversals in the eastern Aleutian arc, *J. Geophys. Res.*, *88*, 9347–9373, doi:10.1029/JB088iB11p09347.
- Housner, G. W., and T. Vreeland Jr. (1966), *The Analysis of Stress and Deformation*, 440 pp., Macmillan, New York.
- Izbekov, P. E., J. F. Larsen, and J. E. Gardner (2005), Petrological and experimental constraints on the recent magma plumbing system at Okmok Volcano, Alaska, USA, *Eos Trans. AGU*, *86*(52), Fall Meet. Suppl., Abstract V13B-0533.
- Jolly, A. D., S. C. Moran, S. R. McNutt, and D. B. Stone (2007), Three-dimensional P wave velocity structure derived from local earthquakes at the Katmai group of volcanoes, Alaska, *J. Volcanol. Geotherm. Res.*, *159*, 326–342, doi:10.1016/j.jvolgeores.2006.06.022.
- Kienle, J., and C. J. Nye (1990), Okmok caldera: Eastern Aleutian islands, in *Volcanoes of North America*, edited by C. A. Wood and J. Kienle, pp. 41–43, Cambridge Univ. Press, Cambridge, U. K.
- Kissling, E., W. L. Ellsworth, D. Eberhart-Phillips, and U. Kradolfer (1994), Initial reference models in local earthquake tomography, *J. Geophys. Res.*, *99*, 19,63–19,646, doi:10.1029/93JB03138.
- Lallement, H. G. A., and J. S. Oldow (2000), Active displacement partitioning and arc-parallel extension of the Aleutian volcanic arc based on Global Positioning System geodesy and kinematic analysis, *Geology*, *28*, 739–742, doi:10.1130/0091-7613(2000)28<739:ADPAAE>2.0.CO;2.
- Larsen, J. F., C. A. Neal, J. R. Schaefer, J. E. Beget, and C. J. Nye (2007), Late Pleistocene and Holocene caldera-forming eruptions of Okmok Caldera, Aleutian Islands, Alaska, in *Volcanism and Subduction: The Kamchatka Region*, *Geophys. Monogr. Ser.*, vol. 172, edited by J. Eichelberger et al., pp. 34–363, doi:10.1029/172GM24, AGU, Washington, D. C.
- Larsen, J., C. Neal, P. Webley, J. Freymueller, M. Haney, S. McNutt, D. Schneider, S. Prejean, J. Schaefer, and R. Wessels (2009), Eruption of Alaska volcano breaks historic pattern, *Eos Trans. AGU*, *90*, 173–180, doi:10.1029/2009EO200001.
- Lin, F.-C., M. P. Moschetti, and M. H. Ritzwoller (2008), Processing seismic ambient noise data to obtain reliable broad-band surface wave dispersion measurements, *Geophys. J. Int.*, *169*, 1239–1260, doi:10.1111/j1365-246X.2008.03720.x.
- Lu, Z., D. Mann, J. T. Freymueller, and D. J. Meyer (2000), Synthetic aperture radar interferometry of Okmok volcano, Alaska: Radar observations, *J. Geophys. Res.*, *105*, 10,791–10,806, doi:10.1029/2000JB900034.
- Lu, Z., E. Fielding, M. R. Patrick, and C. M. Trautwein (2003a), Estimating lava volume by precision combination of multiple baseline spaceborne and airborne interferometric synthetic aperture radar: The 1997 eruption of Okmok volcano, Alaska, *IEEE Trans. Geosci. Remote Sens.*, *41*, 1428–1436.
- Lu, Z., T. Masterlark, D. Dzurisin, R. Rykhus, and C. Wicks Jr. (2003b), Magma supply dynamics at Westdahl volcano, Alaska, modeled from satellite radar interferometry, *J. Geophys. Res.*, *108*(B7), 2354, doi:10.1029/2002JB002311.
- Lu, Z., T. Masterlark, and D. Dzurisin (2005), Interferometric synthetic aperture study of Okmok volcano, Alaska: Magma supply dynamics and post-emplacement lava flow deformation, *J. Geophys. Res.*, *110*, B02403, doi:10.1029/2004JB003148.
- Lysmer, J. (1970), Lumped mass method for Rayleigh waves, *Bull. Seismol. Soc. Am.*, *60*, 89–104.
- Ma, S., G. A. Prieto, and G. C. Beroza (2008), Testing community velocity models for Southern California using the ambient seismic field, *Bull. Seismol. Soc. Am.*, *98*, 2694–2714, doi:10.1785/0120080947.
- Mann, D., J. Freymueller, and Z. Lu (2002), Deformation associated with the 1997 eruption of Okmok volcano, Alaska, *J. Geophys. Res.*, *107*(B4), 2072, doi:10.1029/2001JB000163.
- Massonnet, D., and K. Feigl (1998), Radar interferometry and its application to changes in the Earth's surface, *Rev. Geophys.*, *36*, 441–500, doi:10.1029/97RG03139.
- Masterlark, T. (2007), Magma intrusion and deformation predictions: Sensitivities to the Mogi assumptions, *J. Geophys. Res.*, *112*, B06419, doi:10.1029/2006JB004860.
- Masterlark, T., and Z. Lu (2004), Transient volcano deformation sources imaged with interferometric synthetic aperture radar: Application to Segoum Island, Alaska, *J. Geophys. Res.*, *109*, B01401, doi:10.1029/2003JB002568.
- Masterlark, T., Z. Lu, and R. Rykhus (2006), Thickness distribution of a cooling pyroclastic flow deposit: Optimization using InSAR, FEMs, and an adaptive mesh algorithm, *J. Volcanol. Geotherm. Res.*, *150*, 186–201, doi:10.1016/j.jvolgeores.2005.07.004.
- McCann, G. D., and C. H. Wilts (1951), *A Mathematical Analysis of the Subsidence in the Long Beach—San Pedro Area*, 117 pp., Calif. Inst. of Technol., Pasadena.
- McGimsey, R. G., and K. L. Wallace (1999), 1997 volcanic activity in Alaska and Kamchatka: Summary of events and response of the Alaska Volcano Observatory, *U.S. Geol. Surv. Open File Rep.*, *OF 99-0448*, 42 pp.
- McTigue, D. F. (1987), Elastic stress and deformation near a finite spherical magma body: Resolution of the point source paradox, *J. Geophys. Res.*, *92*, 12,931–12,940, doi:10.1029/JB092iB12p12931.
- Miller, T. P., R. G. McGimsey, D. H. Richter, J. R. Riehle, C. J. Nye, M. E. Yount, and J. A. Dumoulin (1998), Catalog of the historically active volcanoes of Alaska, *U.S. Geol. Surv. Open File Rep.*, *98-582*, 104 pp.
- Miyagi, Y., J. T. Freymueller, F. Kimata, T. Sato, and D. Mann (2004), Surface deformation caused by shallow magmatic activity at Okmok volcano, Alaska, detected by GPS campaigns 2000–2002, *Earth Planets Space*, *56*, e29–e32.
- Mogi, K. (1958), Relations between the eruptions of various volcanoes and the deformations of the ground surface around them, *Bull. Earthquake Res. Inst. Univ. Tokyo*, *36*, 99–134.
- Newman, A. V., T. H. Dixon, G. I. Ofoegbu, and J. E. Dixon (2001), Geodetic and seismic constraints on recent activity at Long Valley Caldera, California: Evidence for viscoelastic rheology, *J. Volcanol. Geotherm. Res.*, *105*, 183–206, doi:10.1016/S0377-0273(00)00255-9.
- Newman, A. V., T. H. Dixon, and N. Gourmelen (2006), A four-dimensional viscoelastic deformation model for Long Valley Caldera, California, between 1995 and 2000, *J. Volcanol. Geotherm. Res.*, *150*, 244–269, doi:10.1016/j.jvolgeores.2005.07.017.
- Okada, Y. (1992), Internal deformation due to shear and tensile faults in a half-space, *Bull. Seismol. Soc. Am.*, *82*, 1018–1040.
- Pagli, C., F. Sigmundsson, T. Arnadóttir, P. Einarsson, and E. Sturkell (2006), Deflation of the Askja volcanic system: Constraints on the deformation source from combined inversion of satellite radar interferograms and GPS measurements, *J. Volcanol. Geotherm. Res.*, *152*, 97–108, doi:10.1016/j.jvolgeores.2005.09.014.
- Patrick, M. R., J. Dehn, K. R. Papp, Z. Lu, K. Dean, L. Moxey, P. Izbekov, and R. Guritz (2003), The 1997 eruption of Okmok volcano, Alaska: A synthesis of remotely sensed imagery, *J. Volcanol. Geotherm. Res.*, *127*, 87–105, doi:10.1016/S0377-0273(03)00180-X.
- Patrick, M. R., J. Dehn, and K. Dean (2004), Numerical modeling of lava flow cooling applied to the 1997 Okmok eruption: Approach and analysis, *J. Geophys. Res.*, *109*, B03202, doi:10.1029/2003JB002537.
- Press, W., S. Teukolsky, W. Vetterling, and B. Flannery (2007), *Numerical Recipes in C: The Art of Scientific Computing*, 3rd ed., 1235 pp., Cambridge Univ. Press, New York.
- Prieto, G. A., and G. C. Beroza (2008), Earthquake ground motion prediction using the ambient seismic field, *Geophys. Res. Lett.*, *35*, L14304, doi:10.1029/2008GL034428.
- Richter, C. F. (1943), Calculation of small distances, *Bull. Seismol. Soc. Am.*, *33*, 243–250.
- Rodi, W. L., P. Glover, T. M. C. Li, and S. S. Alexander (1975), A fast, accurate method for computing group-velocity partial derivatives for Rayleigh and Love modes, *Bull. Seismol. Soc. Am.*, *65*, 1105–1114.
- Romanowicz, B. (2002), Inversion of surface waves, in *International Handbook of Earthquake and Engineering Seismology*, edited by W. H. K. Lee et al., pp. 149–174, Kluwer, Amsterdam.
- Rubin, A. M. (1995), Propagation of magma-filled cracks, *Annu. Rev. Earth Planet. Sci.*, *23*, 287–336, doi:10.1146/annurev.earth.23.050195.001443.
- Ryan, M. P. (1987a), Elasticity and contractancy of Hawaiian olivine tholeiite and its role in the stability and structural evolution of sub-caldera magma reservoirs and volcanic rift systems, in *Volcanism in Hawaii*, edited by R. W. Decker, T. L. Wright, and P. H. Stauffer, *U.S. Geol. Survey Prof. Pap.*, *1350*, vol. 2, 1395–1448.
- Ryan, M. P. (1987b), Neutral buoyancy and the mechanical evolution of magmatic systems, in *Magmatic Processes: Physicochemical Principles*, edited by B. O. Mysen, *Spec. Publ. Geochem. Soc.*, *1*, 259–288.
- Ryan, M. P. (1994), Neutral buoyancy-controlled magma transport and storage in mid-ocean ridge magma reservoirs and their sheeted dike complex: A summary of basic relationships, in *Magmatic Systems*, edited by M. P. Ryan, pp. 97–135, Academic, San Diego, Calif.

- Saccorotti, G., B. Chouet, and P. Dawson (2003), Shallow-velocity models at the Kilauea Volcano, Hawaii, determined from array analysis of tremor wavefields, *Geophys. J. Int.*, *152*, 633–648, doi:10.1046/j.1365-246X.2003.01867.x.
- Savage, J. C. (1983), A dislocation model for strain accumulation and release at a subduction zone, *J. Geophys. Res.*, *88*, 4984–4996, doi:10.1029/JB088iB06p04984.
- Scherbaum, F. (1996), *Of Poles and Zeros: Fundamentals of Digital Seismology*, 268 pp., Kluwer, Dordrecht, Netherlands.
- Shapiro, N. M., M. Campillo, L. Stehly, and M. Ritzwoller (2005), High resolution surface wave tomography from ambient seismic noise, *Science*, *307*, 1615–1618, doi:10.1126/science.1108339.
- Stern, R. J. (2002), Subduction zones, *Rev. Geophys.*, *40*(4), 1012, doi:10.1029/2001RG000108.
- Stevens, N. F., G. Wadge, C. A. Williams, J. G. Morley, J.-P. Muller, J. B. Murray, and M. Upton (2001), Surface movements of emplaced lava flows measured by synthetic aperture radar interferometry, *J. Geophys. Res.*, *106*, 11,293–11,313, doi:10.1029/2000JB900425.
- Trasatti, E., C. Giunchi, and N. Piana Agostinetti (2007), Numerical inversion of deformation caused by pressure sources: Application to Mount Etna (Italy), *Geophys. J. Int.*, *172*, 873–884, doi:10.1111/j.1365-246X.2007.03677.x.
- Turcotte, D. L., and G. J. Schubert (2002), *Geodynamics: Applications of Continuum Physics to Geological Problems*, 2nd ed., 456 pp., Cambridge Univ. Press, New York.
- Wang, H. F. (2000), *Theory of Linear Poroelasticity: With Applications to Geomechanics*, 287 pp., Princeton Univ. Press, Princeton, N. J.
- Winter, J. D. (2001), *An Introduction to Igneous and Metamorphic Petrology*, 697 pp., Prentice Hall, Englewood Cliffs, N. J.
- Yilmaz, O. (1987), *Seismic Data Processing*, 287 pp., Soc. of Explor. Geophys., Tulsa, Okla.

H. Dickinson and T. Masterlark, Department of Geological Sciences, University of Alabama, Tuscaloosa, AL 35487, USA. (masterlark@geo.ua.edu)

T. Fournier, Department of Earth and Atmospheric Sciences, Cornell University, Ithaca, NY 14853, USA.

M. Haney, Geosciences Department, Boise State University, Boise, ID 83725, USA.

C. Searcy, Alaska Volcano Observatory, U.S. Geological Survey, Anchorage, AK 99508, USA.